UNIVERSITY OF CALIFORNIA,
IRVINE

Electronic Characterization of Perylene-Based Oligonucleotide-Inspired Molecular Wires

THESIS

submitted in partial satisfaction of the requirements
for the degree of

MASTER OF SCIENCE

in Chemistry

by

Austin Grant Wardrip

Thesis Committee:
Professor Alon A. Gorodetsky, Chair
Professor Shane Ardo
Professor Jenny Y. Yang

2017

TABLE OF CONTENTS

Page

LIST OF FIGURES

LIST OF TABLES

LIST OF SCHEMES

ACKNOWLEDGMENTS

First and foremost, I would like thank my advisor, Professor Alon. A. Gorodetsky for his guidance and patience over the years. From his advising, I feel I have significantly grown both as a scientist and as a human being.

I also want to thank everyone involved in the Gorodetsky lab past and present: postdocs, graduate students, undergraduates, high school students. Even if our projects never overlapped or if we never spent considerable time together, I have learned so much from you all. There are too many great people to name here, but know that every one of you has left a positive mark on me.

Finally, I want to thank my friends and family for always having my back and supporting my journey through life so far.

ABSTRACT OF THE THESIS

Electronic Characterization of Perylene-Based Oligonucleotide-Inspired Molecular Wires

By

Austin Grant Wardrip

Master of Science in Chemistry

University of California, Irvine, 2017

Professor Alon A. Gorodetsky, Chair

One-dimensional organic molecular wires have emerged as idealized model systems for investigating charge transport mechanisms at 1-10 nm length scales, where the distinction between individual molecules and bulk materials begins to vanish. However, there are significant difficulties associated with the synthesis and electronic characterization of well-defined organic molecular wires. By drawing inspiration from oligonucleotide synthesis, we have developed a facile strategy for the assembly of perylene-based organic semiconductor building blocks in predetermined arrangements on a DNA-like backbone, resulting in molecular wires which have well-defined lengths, geometries, and sequence contexts. We self-assembled monolayers of these wires onto gold substrates and investigated their charge transport properties with both electrochemical and spectroscopic techniques. We found that as we increased the number of perylene building blocks, both the electron transfer and excited-state charge transfer dynamics show unexpected trends, which we rationalize with molecular dynamics and density-functional theory. Our findings hold significance both for fundamentally understanding nanoscale

charge transport phenomena and for the development of new types of biological and molecular electronic devices.

CHAPTER 1 Introduction

1.1 Motivation

Organic semiconductors have been touted as the next generation of electronic materials for renewable energy technologies and molecular electronics, with the potential to replace more traditional inorganic variants, and as such, they have witnessed tremendous advances within the past two decades.[1-15] These once tantalizing advances have been driven in large part by the development of an improved fundamental understanding of structure-function relationships and charge transport phenomena across a broad range of organic semiconductors.[1-15] However, despite this progress, new organic semiconductor materials are still generally discovered/optimized through "trial and error" methods, and the predictive molecular-level design of high-performance organic semiconductors remains intractable.

The difficulties inherent to the *a priori* rational design of organic semiconductor materials for molecular electronics can be visualized by considering the evolution in electronic structure accompanying the transition of an isolated molecule into an extended solid.[8-15] The transition is illustrated for a prototypical one-dimensional organic semiconductor in Figure 1.1A. For this theoretical material, the initial isolated molecular building block features distinct lowest unoccupied molecular orbital (LUMO) and highest occupied molecular orbital (HOMO) energy levels (Figure 1.1A, left). As a multimer is formed from the isolated molecules, non-covalent intermolecular interactions and wave function overlap induce the formation of multiple closely spaced energy levels (Figure 1.1A, middle). Eventually, the incorporation of additional building blocks furnishes a semi-infinite one-dimensional chain with a band-like electronic structure, where the effective

valence and conduction bands possess a finite width (Figure 1.1A, right). For each of the distinct length scales associated with these three regimes (encompassing one to tens to hundreds of nanometers), organic semiconductors often possess radically different behavior and properties,[8-15] making it impossible to generally establish design principles across this class of materials and to specifically predict the functionality that will emerge for any one type of material.

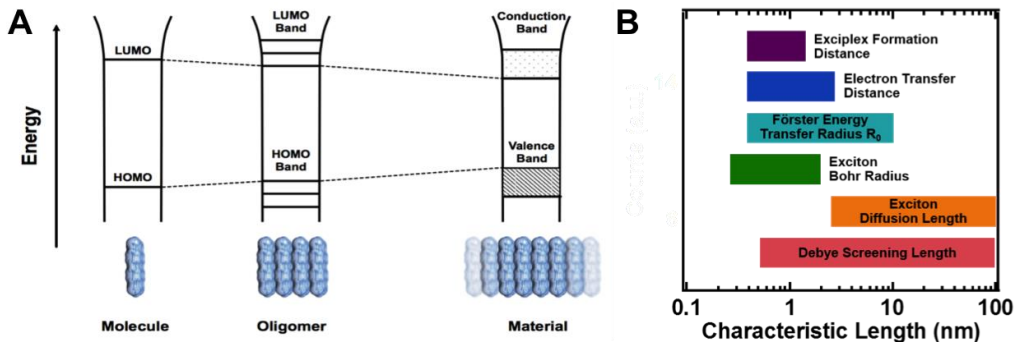

Figure 1.1: (A) Energy diagram depicting the change in electronic structure that accompanies the transition of a molecule into an extended material. The initial molecule (left) features well-defined HOMO and LUMO energy levels, the oligomer (middle) features multiple closely spaced energy levels, and the extended material (right) features a band-like electronic structure. (B) The characteristic length scales associated with charge transfer/transport various phenomena in organic semiconductor materials.

From the perspective of rational organic semiconductor design, the length regime of 1-10 nanometers associated with multimeric ensembles hold particular relevance because not only are electronic devices at this size, it encompasses many key charge transport phenomena, such as exciplex formation, electron transfer, Förster energy transfer, exciton generation, and exciton Bohr radius, among others (Figure 1.1B).[11] However, the study of such ensembles has remained notoriously difficult for several reasons.[1-15] First, traditional

self-assembly or fabrication techniques are poorly suited for the preparation of general model systems where the length, molecular building block sequence, overall geometry, and terminal functionalities are well defined. Second, the tens of nanometers length regime is technically challenging to study with multiple techniques that furnish complementary information within a single context, especially when requiring simultaneous excellent chemical, temporal, and spatial resolution. Third, the weak short-range non-covalent interactions that govern the properties of such systems are notoriously difficult to enforce and reliably assess, with even subtle changes in the interactions often yielding dramatic and unexpected effects. Thus, a general methodology for the construction and experimental evaluation of precisely defined constructs, which emulate the properties of organic semiconductors in the tens of nanometers length regime, remains as an important unmet challenge.

1.2 Overview of the Thesis

We address the above challenge through the design, preparation, and characterization of a novel class of one-dimensional bioinspired organic semiconductor molecular wires. In Chapter 2, we rationally design our organic molecular wires by drawing upon concepts from the organic electronics and oligonucleotide chemistry fields. We then synthesize a specific perylene-based small molecular building block and prepare/purify length-variable oligonucleotide-like constructs via traditional bioconjugate chemistry techniques. We next evaluate the geometries and architectures of these molecular wires with molecular dynamics simulations and x-ray diffraction methods. We in turn self-assemble the molecular wires into ordered monolayers, which we chemically and

structurally characterize with x-ray photoelectron and near edge x-ray absorption spectroscopy. We subsequently investigate charge transport through our surface-bound constructs with a synergistic combination of cyclic voltammetry. In Chapter 3, we further investigate charge transport using resonance photoemission spectroscopy. We finally evaluate the electronic structures of the molecular wires with density functional theory and develop models that rationalize their charge transport properties. In Chapter 4, a brief summary is given along with future work this project will have involving repeating this entire systematic set of studies for sequence-variable molecular wires from different perylene-based molecular building blocks.

1.3 References

1) Sirringhaus, H. 25th Anniversary Article: Organic Field-Effect Transistors: The Path Beyond Amorphous Silicon. *Adv. Mater.* **2014**, *26* (9), 1319–1335.
2) Dong, H.; Fu, X.; Liu, J.; Wang, Z.; Hu, W. 25th Anniversary Article: Key Points for High-Mobility Organic Field-Effect Transistors. *Adv. Mater.* **2013**, *25* (43), 6158–6183.
3) Dou, L.; You, J.; Hong, Z.; Xu, Z.; Li, G.; Street, R. A.; Yang, Y. 25th Anniversary Article: A Decade of Organic/Polymeric Photovoltaic Research. *Adv. Mater.* **2013**, *25* (46), 6642–6671.
4) National Renewable Energy Laboratory Best Research-Cell Efficiencies http://www.nrel.gov/ncpv/images/efficiency_chart.jpg, (accessed Aug 1, 2015).
5) Hwang, J.; Wan, A.; Kahn, A. Energetics of Metal–organic Interfaces: New Experiments and Assessment of the Field. *Mater. Sci. Eng. R Reports* **2009**, *64* (1–2), 1–31.
6) Braun, S.; Salaneck, W. R.; Fahlman, M. Energy-Level Alignment at Organic/metal and Organic/organic Interfaces. *Adv. Mater.* **2009**, *21* (14–15), 1450–1472.
7) Liu, C.; Xu, Y.; Noh, Y. Y. Contact Engineering in Organic Field-Effect Transistors. *Mater. Today* **2015**, *18* (2), 79–96.
8) Cropceanu, V.; Cornil, J.; da Silva Filho, D. A.; Olivier, Y.; Silbey, R.; Bredas, J.-L. Charge Transport in Organic Semiconductors. *Chem. Rev.* **2007**, *107*, 926–952.
9) Kymissis, I. *Organic Field Effect Transistors: Theory, Fabrication, and Characterization*; Springer: New York, **2009**.
10) Tessler, N.; Preezant, Y.; Rappaport, N.; Roichman, Y. Charge Transport in Disordered Organic Materials and Its Relevance to Thin-Film Devices: A Tutorial Review. *Adv. Mater.* **2009**, *21* (27), 2741–2761.

11) Kim, F. S.; Ren, G.; Jenekhe, S. A. One-Dimensional Nanostructures of π-Conjugated Molecular Systems: Assembly, Properties, and Applications from Photovoltaics, Sensors, and Nanophotonics to Nanoelectronics. *Chem. Mater.* **2011**, *23* (3), 682–732.
12) Rivnay, J.; Mannsfeld, S. C. B.; Miller, C. E.; Salleo, A.; Toney, M. F. Quantitative Determination of Organic Semiconductor Microstructure from the Molecular to Device Scale. *Chem. Rev.* **2012**, *112* (10), 5488–5519.
13) *Physics of Organic Semiconductors*; Brütting, W., Adachi, C., Eds.; Wiley-VCH Verlag GmbH & Co. KGaA: Weinheim, Germany, **2013**.
14) Puniredd, S. R.; Pisula, W.; Müllen, K. Influence of film morphology on optical and electronic properties of organic materials. in *Handbook of Organic Materials for Optical and (Opto)Electronic Devices,* Ostroverkhova, O., Ed.; Philadelphia, 2013, 83–101.
15) Köhler, A.; Bässler, H. *Electronic Processes in Organic Semiconductors: An Introduction*; Wiley-VCH: Weinheim, Germany, 2015.

CHAPTER 2 Length-Independent Charge Transport in Chimeric Molecular Wires

2.1 Abstract

Advanced molecular electronic components remain vital for the next generation of miniaturized integrated circuits. Thus, much research effort has been devoted to the discovery of lossless molecular wires, for which the charge transport rate or conductivity is not attenuated with length in the tunneling regime. Herein, we report the synthesis and electrochemical interrogation of DNA-like molecular wires. We determine that the rate of electron transfer through these constructs is independent of their length and propose a plausible mechanism to explain our findings. The reported approach holds relevance for the development of high-performance molecular electronic components and the fundamental study of charge transport phenomena in organic semiconductors.

2.2 Introduction

Molecular electronic devices have the potential to redefine integrated circuit technologies and transform modern computing.[1-2] Consequently, much effort has focused on the discovery and study of π-conjugated molecular wires (notable examples include oligoporphyrins, oligophenylenevinylenes, and DNA) that efficiently transport charge at length scales of $< \sim 5$ nm, which corresponds to both the tunneling regime of charge transport and the limits of modern lithography.[3-11] Typically, such wires or bridges are electrically interrogated in various configurations, i.e. scanning probe break junctions,[12,13] two terminal devices,[14,15] and self-assembled monolayers,[16,17] with the measurements yielding information on their ground state charge transport properties. However, for many

of the molecular wires reported to date, the charge transport rate (i.e. conductivity) drops off precipitously with length in the tunneling transport regime.[12-21] Furthermore, artificial molecular wires are often difficult to synthesize, while natural molecular wires can exhibit poor stability during repeated electrical interrogation.[12-21] Consequently, given recent impressive advances in the miniaturization of transistors and integrated circuits,[22] the development of modular, sequence-controlled molecular wires that efficiently transport charge at length scales of < ~ 5 nm remains of paramount importance.

Herein, we describe the synthesis and electrochemical characterization of chimeric molecular wires. First, we draw upon concepts from the oligonucleotide chemistry and organic electronics fields to synthesize a series of bioinspired macromolecules. We in turn self-assemble these constructs into monolayers and evaluate their orientations with X-ray spectroscopic techniques. Subsequently, we investigate the monolayers' electrochemical properties, and from our measurements, we extract the rate of electron transport through the molecular wires, finding that it is independent of their length. We in turn rationalize our observations with density functional theory (DFT) calculations and propose a mechanism to explain our findings. Our approach may provide opportunities for the development of high-performance molecular electronic components and for the study of charge transport phenomena within organic, biological, and bioinspired materials.

2.3 Results and Discussion

We began our experiments by drawing inspiration from the organic electronics and oligonucleotide chemistry fields for the rational design and preparation of the macromolecules illustrated in Figure 1A. Here, we selected perylene-3,4,9,10

tetracarboxylic diimide (PTCDI) as the π-conjugated building block for our constructs because this molecule possesses well-known electrochemical properties, a propensity for adapting stacked columnar-like arrangements, and excellent stability under varied conditions.[23,24] Next, we used standard automated oligonucleotide chemistry techniques, which are compatible with PTCDI derivatives,[25-30] to produce, purify, and characterize thiol and ferrocene-modified macromolecules featuring one, two, three, or four PTCDIs arranged on an alkane-phosphate backbone (see the Supporting Information for details). The final designer systems, which we denoted as **P1**, **P2**, **P3**, or **P4**, consisted of variable-length PTCDI tracts as the conductive bridge components, terminal thiol linkers as handles for monolayer formation, and pendant ferrocene moieties as redox probes of charge transport (Figure 2.1A).

We proceeded to self-assemble and spectroscopically characterize monolayers from **P1**, **P2**, **P3**, or **P4**. Thus, as illustrated in Figure 2.1B, we incubated clean gold substrates with solutions of each of our thiol-modified constructs, allowing for formation of specific covalent S-Au bonds, and then treated the modified substrates with mercaptohexanol to displace non-specifically physisorbed species.[16,17,29,31-33] In turn, we interrogated the four backfilled monolayers with near edge X-ray absorption fine structure spectroscopy (NEXAFS), collecting partial electron yield spectra with the incident electric fields parallel and perpendicular to the substrate surface (Figures S2.6 to S2.9).[34] Based on literature precedent for PTCDI-based materials, we assigned the spectras' characteristic inequivalent doublets at energies between 284 eV and 286 eV to carbon 1s→π* transitions that are localized on the aromatic core of PTCDIs and associated with the LUMO (left doublet) and LUMO+1 (right doublet) (SI Figures S2.6 to S2.9).[35] By evaluating the dependence of these

signals' intensities on the polarization of the electric field, we calculated average substrate-relative tilt angles of ~ 61 ± 2°, ~ 61 ± 2°, ~ 60 ± 2°, or ~ 60 ± 2° for the constituent PTCDIs of monolayers from **P1**, **P2**, **P3**, or **P4**, respectively. Overall, the NEXAFS experiments indicated that our monolayers' constituent macromolecules adopted nearly identical upright orientations, in analogy to duplexes in backfilled DNA monolayers.[10,29,33]

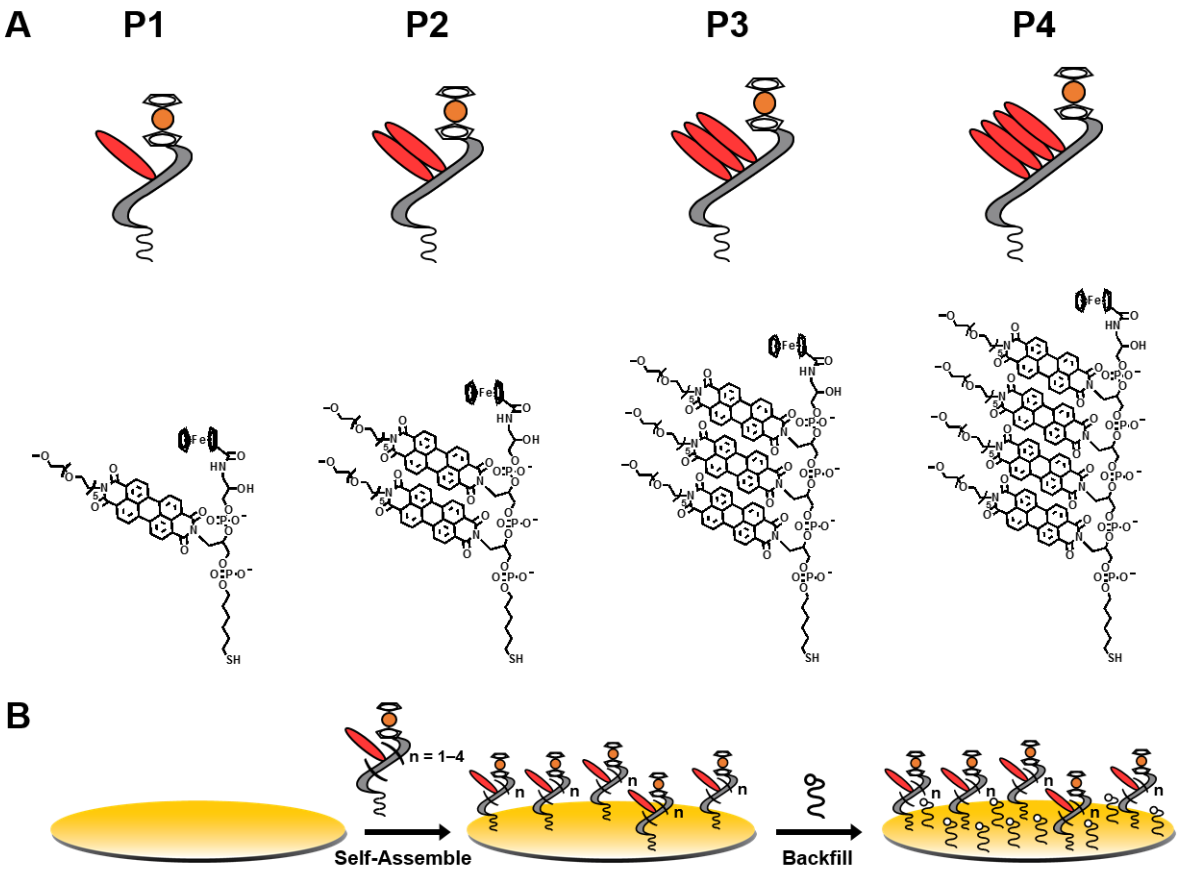

Figure 2.1. (A) Illustration (top) and chemical structure (bottom) for macromolecules **P1**, **P2**, **P3**, and **P4**, which consist of tracts of one to four PTCDIs arranged on an alkane-phosphate backbone and flanked by thiol-terminated saturated linkers and ferrocene-terminated saturated tethers. (B) Illustration of the formation of self-assembled monolayers from the macromolecules in (A).

As an initial control, we investigated the electrochemical properties of backfilled monolayers from **P0**, which is an analogue of our macromolecules but lacks any PTCDIs (SI Figures S23). Here, we observed a redox couple at a potential of ~ 0.46 V (±0.002) mV vs. Ag/AgCl, which we attributed to the pendant ferrocene moiety (Figure S2.5).[16,17,36-38] This couple featured an anodic to cathodic peak current ratio of 1.07 (±0.04), indicating a quasi-reversible redox reaction, and a linear dependence of the anodic peak current on the scan rate, indicating a surface bound species (Figure S2.5C).[17,39] Moreover, from the anodic wave, we calculated a surface coverage of ~ 22 (±4) pmol/cm^2, which was smaller than the estimated maximum coverages of ~300 and ~450 pmol/cm^2 for DNA and ferrocene-terminated alkanethiol monolayers, respectively,[40,41] as well as a full width at half maximum (FWHM) of 0.14 (±0.004) V, which was greater than the ideal value of ~ 0.091 V.[17,39] These metrics suggested a relatively dilute monolayer, likely due to the presence of repulsive electrostatic interactions between our constructs' negatively-charged backbones.[17,39] Altogether, our measurements demonstrated that backfilled monolayers from **P0** generally resembled analogous ones from ferrocene-terminated alkanethiols reported in the literature.[16,17,36-38]

We next evaluated the rate of electron transfer between the pendant ferrocene moieties and the gold electrode for **P0**, as mediated by the phospho-alkane bridge. By analyzing the cyclic voltammograms obtained at different scan rates, we extracted the electron transfer rate constant k_0 according to the Laviron approach (see the Supporting Information for details).[17,42] The calculated k_0 value for **P0** was 9.7 (±1) x 10^2 s^{-1} (corresponding to a probe-electrode through-bond distance of 2.29 nm). This value was in good agreement with rate constants of k_0 = 6.0 x 10^3 s^{-1}, k_0 = 1.2 x 10^3 s^{-1}, and k_0 = 1.0 x 10^2

s^{-1} reported for analogous ferrocene-terminated alkanethiol monolayers (corresponding to probe-electrode through-bond distances of 1.84 nm, 2.00 nm, and 2.47 nm, respectively) (Table 2.1).[36-38] Our observations and analysis indicated that non-resonant tunneling was the likely mechanism governing electron transport through monolayers from **P0**.

Ferrocene Species	ET Rate k_0 (s^{-1})	ET Distance (nm)[a]	Reference
$FcCONH(CH_2)_7SH$	6.6×10^4	1.53	37
$FcCONH(CH_2)_8SH$	1.5×10^4	1.69	37
$FcCONH(CH_2)_9SH$	6.0×10^3	1.84	37
$FcCONH(CH_2)_{10}SH$	1.2×10^3	2.00	37
$FcCO_2(CH_2)_{13}SH$	1.0×10^2	2.47	36
$Fc(CH_2)_{16}SH$	2.8×10^1	2.65	38
$FcCONH(CH_2)_{15}SH$	7.0×10^0	2.77	37
P0	$9.7\ (\pm1) \times 10^2$	2.29	This work
P1	$8.2\ (\pm1) \times 10^2$	3.05	This work
P2	$8.3\ (\pm0.8) \times 10^2$	3.81	This work
P3	$8.8\ (\pm1) \times 10^2$	4.57	This work
P4	$8.2\ (\pm0.8) \times 10^2$	5.33	This work

Table 2.1. Various ferrocene-terminated species (Column 1), along with the corresponding electron transfer rate constants k_0 (Column 2) and through-bond electron transfer distances (Column 3). [a] Electron transfer (ET) distance is defined as the sum of all the bond lengths between the pendant ferrocene redox probe and the terminal gold-bound sulfur atom.

We continued our studies by investigating the electrochemical properties of backfilled monolayers from **P1**, **P2**, **P3**, or **P4** at positive potentials vs. Ag/AgCl (Figure 2.2). These monolayers featured reversible redox couples at potentials of approximately ~

0.47 to ~ 0.52 V vs. Ag/AgCl, anodic to cathodic peak current ratios of ~ 1.02 to ~1.16, anodic FWHMs of 0.13 V, average surface coverages of ~ 20 pmol/cm^2 to ~ 25 pmol/cm^2, and linear plots of peak current as a function of scan rate (Figure S2.11 and Table S2.1). Altogether, our measurements indicated that the electrochemical characteristics of monolayers from **P1**, **P2**, **P3**, and **P4** closely resembled not only those of **P0** but also one another.

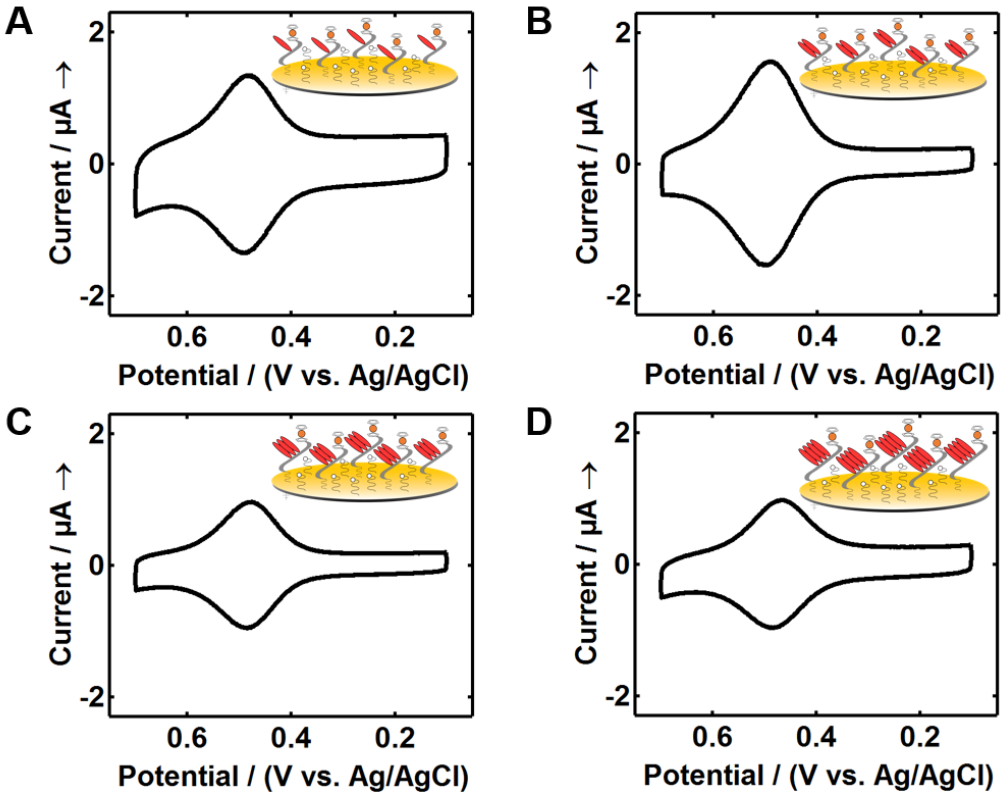

Figure 2.2. Cyclic voltammograms at positive potentials for mercaptohexanol-backfilled monolayers from (A) **P1**, (B) **P2**, (C) **P3**, and (D) **P4**. The insets show schematics of the corresponding monolayers.

We further explored the electrochemical properties of backfilled monolayers from **P1**, **P2**, **P3**, or **P4** at negative potentials vs. Ag/AgCl (Figure 2.3). We found one to three quasi-reversible redox couples for **P1**, **P2**, **P3**, and **P4**, with a midpoint potential of approximately ~ –0.4 V vs. Ag/AgCl for the initial (least negative) couple in each instance. Based on literature precedent for PTCDIs,[23,24,31] we attributed these redox signatures to the macromolecules' LUMOs (and energetically similar orbitals), and by using the pendant ferrocenes as internal standards,[39] we calculated reliable LUMO energies of –4.11 (±0.006) eV, –4.15 (±0.01) eV, –4.19 (±0.007) eV, and –4.22 (±0.005) eV for **P1**, **P2**, **P3**, and **P4**, respectively. Here, the lowering of the LUMO energies and appearance of multiple energetically similar states for the longer macromolecules indicated the likely presence of strong interactions between the constituent PTCDIs. Overall, the electrochemical measurements suggested that the PTCDI substructures essentially behaved as single electroactive units.

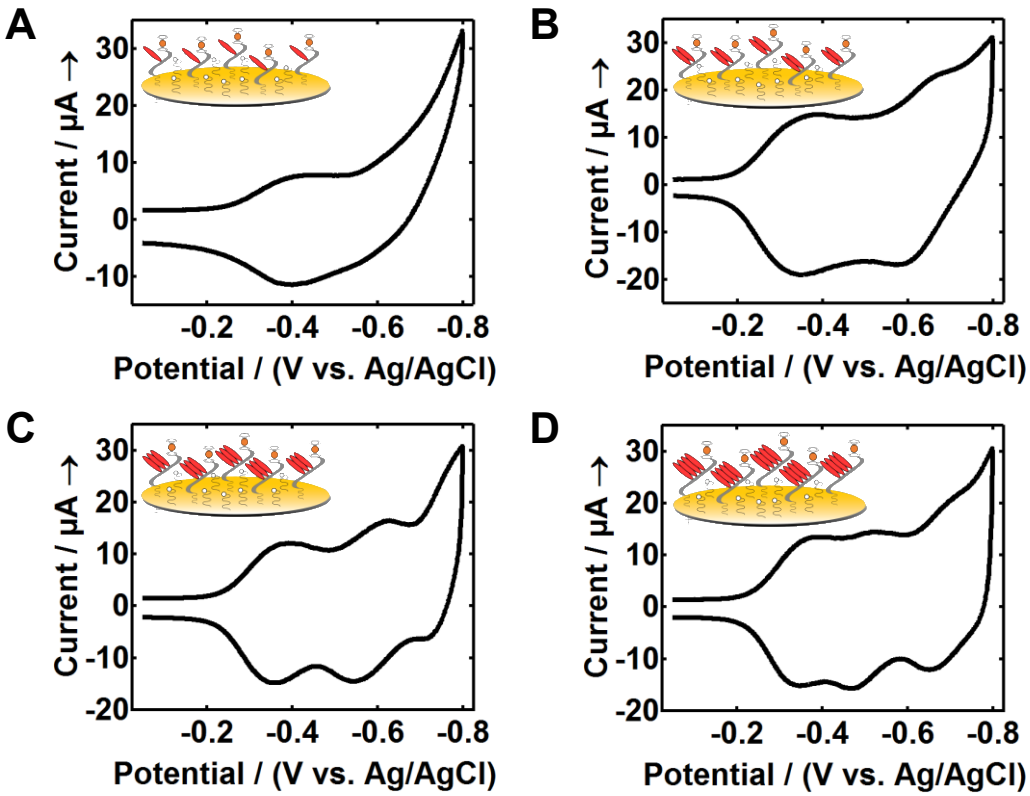

Figure 2.3: Cyclic voltammograms at negative potentials for mercaptohexanol-backfilled monolayers from (A) **P1**, (B) **P2**, (C) **P3**, and (D) **P4**. The inserts show schematics of the corresponding molecular wires.

We next evaluated the rate of electron transfer through backfilled monolayers from **P1**, **P2**, **P3**, or **P4**. Here, the PTCDI-based substructures, along with their terminal tethers and linkers, served as extended spacers or bridges between the pendant ferrocene moieties and the gold electrodes. From an analysis of cyclic voltammograms obtained at different scan rates for **P1**, **P2**, **P3**, and **P4** monolayers, we extracted these macromolecules' respective electron transfer rate constants (see the Supporting Information for details). Surprisingly, for **P1**, we found only a small decrease in the electron transfer rate constant k_0 to 8.2 (±1) x 10^2 s^{-1}, despite the much larger probe-electrode through-bond distance of

3.05 nm (relative to **P0**) (Table 2.1). This value was in stark contrast to the much slower rate constants of 2.8 x 10^1 s^{-1} and 7.0 x 10^0 s^{-1} found for ferrocene-terminated alkanethiol monolayers with probe-electrode through-bond distances of 2.65 nm and 2.77 nm, respectively (Table 2.1).[36-38] Furthermore, we found that the electron transfer rate remained virtually unchanged for the longer macromolecules, with values of 8.3 (±0.8) x 10^2 s^{-1} for **P2**, 8.8 (±1) x 10^2 s^{-1} for **P3**, and 8.2 (±0.8) x 10^2 s^{-1} for **P4**, despite the substantially increased probe-electrode distances of 3.81 nm for **P2**, 4.57 nm for **P3**, and 5.33 nm for **P4**, respectively (Table 2.1). Together, the measurements indicated that rate of electron transport through our molecular wires was effectively not attenuated with length.

To facilitate interpretation of our experimental observations, we performed density functional theory (DFT) calculations. Thus, we first adapted our reported protocols[30] and used molecular dynamics simulations to obtain the lowest free energy (most thermodynamically stable) atomistic conformations for the PTCDI-based substructures of **P1**, **P2**, **P3**, and **P4** (Figure S2.13). In turn, we employed the simulated equilibrium geometries and the long-range-corrected CAM-B3LYP functional[43] within the Gaussian 09 package to generate the shapes and energies of our four macromolecules' highest occupied molecular orbitals (HOMOs) and lowest unoccupied molecular orbitals (LUMOs) (Figure S2.14). Here, we found that the electron density was delocalized over either the entirety or majority of the substructures' aromatic cores, demonstrating that their constituent PTCDI moieties were not electronically independent of one another (presumably due to through-space intramolecular electronic coupling). Moreover, in agreement with the experimental observations, we found that the theoretically-predicted LUMO energies were lowered for the longer macromolecules, with values of –2.66 eV, –3.01 eV, –3.36 eV, and –3.36 eV for

P1, **P2**, **P3**, and **P4**, respectively (note that the values do not perfectly match the experimental observations due to the limited accuracy of the functional and the exclusion of solvent and/or substrate effects). Overall, the calculations shed insight into the electronic structure of our constructs and provided a rationale for their electrochemical behavior as single electroactive units.

Our experimental and computational observations warrant a discussion of the likely mechanism governing electron transport for **P1**, **P2**, **P3**, and **P4**. Here, we note that our macromolecules consist of several distinct components: π-stacked PTCDI-based substructures, primarily saturated tethers bound to the electrode, and primarily saturated linkers to the pendant ferrocene probes (Figure 2.1A). Based on previous findings for monolayers from ferrocene-terminated alkanethiols[16,17,36-38] (as well as on our experimental observations for monolayers from **P0**), electrons are likely transported through the tethers and linkers of our macromolecules via a rate-limiting and lossy non-resonant tunneling mechanism.[16-21] Furthermore, based on reports of extremely rapid electron hopping rates of $> 10^7$ s^{-1}[28] and femtosecond exciton dissociation times in analogous PTCDI-based ensembles,[44] (as well as our computational observations for **P1**, **P2**, **P3**, and **P4**), electrons are likely transported through the PTCDI substructures of our macromolecules via a rapid and nearly lossless resonant tunneling mechanism.[16-21] The combination of these two mechanisms accounts for the observation of length-independent charge transport in our macromolecules.[12-21]

2.4 Conclusion

In conclusion, we have synthesized a series of chimeric molecular wires and characterized their charge transport properties. Our study holds significance for several reasons. First, the reported synthetic methodology employs straightforward, readily accessible bioconjugate chemistry techniques to prepare well-defined PTCDI-based molecular wires. In principle, this approach possesses few limitations and could be used to prepare a wide variety of modular, sequence-variable constructs from arbitrary organic semiconductor building blocks. Second, our electrochemical strategy makes it possible to both study charge transport phenomena and to directly monitor changes in electronic structure for sequence-variable molecular wires. Such experimental flexibility underscores the value of our approach for the systematic study of nanoscale charge transport phenomena. Finally, our measurements reveal that the rate of electron transport through our π-stacked molecular wires is not attenuated with length. Given their intrinsic modularity, our macromolecules may thus prove valuable as archetypes for the construction of novel high-performance molecular wires. Altogether, our methodology holds broad significance within the context of molecular, organic, and biological electronics and may afford new opportunities for the development of sophisticated bioinspired molecular electronic components.

2.5 Supporting Information

2.5.1 Materials and Reagents

All general chemical reagents were purchased from Acros Organics, Sigma-Aldrich, or Combi-Blocks. The solvents were obtained from Fisher Scientific and used as received,

unless otherwise noted. Flash chromatography was performed using SiliCycle Silica Flash F60 silica gel. The specific chemical reagents and commercial phosphoramidites required for the automated synthesis steps were purchased from either Glen Research, Inc. or FIVEphoton Biochemicals, Inc. and used as received.

2.5.2 General Procedures for Characterization of the Small Molecule Precursors

All intermediates and products for the phosphoramidite synthesis were characterized with nuclear magnetic resonance (NMR) spectroscopy and mass spectrometry. The electrospray mass spectrometry (ESI MS) data were obtained at the University of California, Irvine Mass Spectrometry Facility on a Waters LCT Premier electrospray time-of-flight instrument. The ^{1}H NMR spectra were obtained on either a Bruker DRX500 or an AVANCE600 instrument. The ^{13}C NMR spectra were obtained on a Bruker DRX500 outfitted with a CryoProbe (Bruker TCI 500 MHz, 5 mm diameter tubes). The ^{31}P NMR spectra were acquired on a Bruker AVANCE600 instrument. Chemical shifts were reported in ppm for ^{1}H, ^{13}C, ^{19}F, and ^{31}P NMR. The chemical shifts for the NMR data were referenced as follows: for samples in $CDCl_3$, the ^{1}H NMR spectra were referenced to tetramethylsilane (TMS) at 0.00, and the ^{13}C NMR spectra were referenced to $CDCl_3$ at 77.23; for samples in CD_3OD, the ^{13}C NMR spectra were referenced to the solvent peak at 49.00; for samples in CD_2Cl_2, the ^{1}H NMR spectra were referenced to the solvent peak at 5.32, and the ^{13}C NMR spectra were referenced to the solvent peak at 54.00. The chemical shifts for the ^{31}P NMR spectra were corrected and referenced by using ^{1}H NMR according to the 2008 IUPAC recommendations.[45] The data are labeled as follows: chemical shift,

multiplicity (s = singlet, d = doublet, t = triplet, q = quartet, quint = quintet, m = multiplet, br s = broad singlet), the coupling constants (in Hertz), and the integration value.

2.5.3 Synthesis and Chemical Characterization of the Molecular Wires

Macromolecules **P0**, **P1**, **P2**, **P3**, and **P4** were synthesized on solid support according to standard commercial protocols recommended by Glen Research, Inc. for an Applied Biosystems (ABI) 394 DNA synthesizer. The synthesis cycle was modified to omit the capping step and to use extended coupling times for the incorporation of both the thiol modifier C6 S-S phosphoramidites and perylenediimide (PTCDI) phosphoramidites, as previously described.[S2,S3] After synthesis, the macromolecules were cleaved from the support by treatment with aqueous ammonium hydroxide and purified *via* reverse phase high performance liquid chromatography (HPLC) on an Agilent 1260 Infinity system, equipped with an Infinity Series diode array detector. Macromolecule **P0** was eluted with a gradient evolved from 95% solvent A and 5% solvent B to 0% solvent A and 100% solvent B over a period of 35 min at a flow rate of 1 mL/min (solvent A, 50 mM ammonium acetate, pH = 6 buffer; solvent B, acetonitrile) on an Agilent Eclipse Plus C18 column. Macromolecules **P1**, **P2**, **P3**, and **P4** were eluted with a gradient evolved from 40% solvent A and 60% solvent B to 0% solvent A and 100% solvent B over a period of 120 min at a flow rate of 1 mL/min (solvent A, 50 mM ammonium acetate, pH = 6 buffer; solvent B, methanol) on an Agilent ZORBAX Stable Bond Phenyl column. The ESI^- MS data were obtained at the University of California, Irvine Mass Spectrometry Facility on a Waters LCT Premier electrospray time-of-flight instrument. The MALDI-TOF mass spectra of the macromolecules were obtained on an Applied Biosystems Sciex MALDI-TOF/TOF 5800

series mass spectrometer in reflectron negative mode, using a 349 nm Nd:YAG laser as the illumination source. The simulated MALDI TOF and ESI^- MS spectra were generated using AB Sciex Data Explorer. A representative HPLC chromatogram and ESI-MS spectrum for **P0** are shown in Figure S2.5, and representative HPLC chromatograms and MALDI-TOF mass spectra for **P1**, **P2**, **P3**, and **P4** are shown in Figures S2.1 to S2.4.

2.5.4 Self-Assembly of Mixed Monolayers from the Molecular Wires

Monolayers from macromolecules **P0, P1**, **P2**, **P3**, and **P4** were formed on polycrystalline gold rod electrodes (Ø = 2 mm; CH Instruments) according to previously reported protocols.[S4] The gold electrodes were freshly prepared before each experiment through sequential polishing with wet alumina slurries (Buehler; particle sizes: 1.0, 0.3, and 0.05 μm) on polishing cloth (Buehler). The electrodes were then electrochemically etched, thoroughly rinsed with MilliQ water, and dried under argon, the macromolecules were self-assembled from methanol over a period of 16 to 24 hours. The monolayers were in turn backfilled with 1 mM mercaptohexanol, displacing non-specifically bound macromolecules. The monolayers were used for electrochemical measurements immediately after backfilling.

2.5.5 X-ray Spectroscopy of Mixed Monolayers from the Molecular Wires.

X-ray spectroscopy experiments were performed at the ALOISA beamline of the Elettra Synchrotron in Trieste, Italy in an ultra-high vacuum end station.[47] During the experiments, the sample temperature was maintained at –60 °C, and the measurement and sample preparation chamber pressures were maintained at 10^{-11} mbar and 10^{-10} mbar,

respectively. The backfilled monolayers were characterized using near edge X-ray absorption fine structure spectroscopy (NEXAFS), which was performed in Partial Electron Yield mode at a grazing-incidence angle of 6° and with the high pass kinetic energy filter set to 250 eV.[48] The resulting spectra were normalized with respect to the beam current measured on the gold coating of the last refocusing mirror. The data obtained for all of the measurements were analyzed and processed according to established literature procedures.[49-52]

2.5.6 Electrochemistry of Mixed Monolayers from the Molecular Wires

Cyclic voltammetry (CV) measurements for monolayers from macromolecules **P0**, **P1**, **P2**, **P3**, and **P4** were performed in a standard three-electrode electrochemical cell with a CHI832C Electrochemical Analyzer (CH Instruments). In a typical experiment, a gold rod electrode (CH Instruments) modified with the relevant mixed monolayer served as the working electrode, a coiled platinum wire (ThermoFisher) served as the counter electrode, and a commercial Ag/AgCl electrode (CH Instruments) served as the reference electrode. The electrochemical measurements were performed under an inert argon atmosphere in an aqueous 0.1 M sodium perchlorate, 2.5 mM sodium phosphate, pH = 7 buffer. The resulting cyclic voltammograms were evaluated according to established protocols.

2.5.7 Calculation of the Electron Transfer Rate Constants

The standard electron transfer rate constants k_0 for mercaptohexanol-backfilled monolayers from macromolecules **P0**, **P1**, **P2**, **P3**, and **P4** were determined by following

the Laviron approach for surface-bound redox-active species undergoing a reversible one-electron transfer process.[S5] For each of the monolayers, cyclic voltammograms were collected at scan rates between 1 and 4000 V s^{-1}, and the voltammograms that satisfied the criterion of kinetic overpotentials of $\eta = (E_p - E^{0'}) > 100$ mV were used for the calculations. In this limiting regime, the dependence of the overpotential on the natural logarithm of the scan rate ln(v) is given by the equations:

$$E_{pa} - E^{0'} = \left(\frac{RT}{(1-\alpha)nF}\right) ln\left(\frac{(1-\alpha)nF}{RTk_f}\right) + \left(\frac{RT}{(1-\alpha)nF}\right) \ln v$$

and

$$E_{pc} - E^{0'} = -\left(\frac{RT}{\alpha nF}\right) ln\left(\frac{\alpha nF}{RTk_b}\right) - \left(\frac{RT}{\alpha nF}\right) \ln v$$

where E_{pa} is the potential of the anodic peak, E_{pc} is the potential of the cathodic peak, v is the scan rate, α is the electron transfer coefficient, k_f is the forward rate constant, k_b is the backward rate constant, R is the ideal gas constant, T is the absolute temperature, F is the Faraday constant, and n is the number of electrons transferred. These equations were used to formulate a plot of the overpotential η versus ln v, which featured linear regions with $\eta >$ 100 mV; as an example, a typical plot for **P0** (including a fit of the linear regions) is shown in Figure S2.10. The electron transfer coefficients α were obtained from the slope of the fits to the linear regions. The electron transfer rate constants k_0 were obtained from the x-intercepts of the linear regions, which correspond to scan rates v_a and v_c where $\eta = 0$ for the anodic and cathodic plots, respectively, and are defined by the equation:

$$k_0 = \frac{\alpha nF v_c}{RT} = \frac{(1-\alpha)nF v_a}{RT}$$

The reported k_0 values correspond to an average of the electron transfer rate constants obtained from the anodic and cathodic plots, which exhibited minor differences (< 50 s^{-1}).

2.5.8 Molecular Dynamics Simulations for the PTCDI-Based Substructures of the Molecular Wires

The molecular dynamics simulations for the PTCDI-based substructures for molecular wires **P1**, **P2**, **P3**, and **P4** were performed with GAFF in NAMD 2.9. The simulations employed the Generalized Born Implicit Solvent model (GIBS) and a monovalent salt concentration of 0.115 M. For the simulations, the substructures of **P1**, **P2**, **P3**, and **P4** featuring the full length side chains (Figure S2.12) were parameterized according to established literature protocols[30] and were in turn used for the molecular dynamics simulations. For each simulation, the starting configuration was obtained by turning off the attractive van der Waals interactions in the force field and setting the temperature to 500 K, thereby ensuring that all PTCDI moieties were completely separated from one another in an unstacked random open configuration. To initiate the simulation, the attractive van der Waals interactions were turned on, and the initial temperature was set to 300 K. All of the simulations were performed at a constant temperature of 300 K for 20 ns, ensuring that steady state was reached. The simulations were analyzed by monitoring the relative center of mass (COM) distances and offset angles for every pair of PTCDIs.[30] The COM distances were calculated from the atomic coordinates and atomic mass of the individual PTCDIs. Here, the offset angles were obtained by constructing a vector from the nitrogen closest to the backbone to the nitrogen farthest from the backbone for the individual PTCDIs. The dot product of these vectors for every pair of

PTCDIs defined the offset angles used for the analysis. The COM distances and offset angles indicated the relative separation and alignment of the PTCDIs, respectively, yielding the geometries in Figure S2.13.

2.5.9 Density-Functional Theory Calculations for the Substructures of the Molecular Wires

Ground state density functional theory calculations for the substructures of **P1**, **P2**, **P3**, and **P4** were performed in Gaussian 09.[53] The averaged structures from the molecular dynamics simulations were used for the substructure geometries. For computational simplicity, the DFT calculations studied PTCDIs that were substituted with methyl groups (rather than hexaethyleneglycol monomethyl ether) at the imide positions opposite to the phosphate backbone. The atomic orbitals were expanded in the cc-pVTZ and 6-31G(d,p) basis sets, and the ground state calculations were performed with all combinations of the aforementioned basis sets, as well as the CAM=B3LYP,[43] B3LYP, and LC-wPBE functionals. The results we report utilize the CAM-B3LYP functional and the cc-pvtz basis set. The molecular orbitals were obtained in Gaussian 09 for the HOMO and LUMO of each PTCDI-based macromolecule (Figure S2.14). The isosurface plots were rendered in VESTA.[54]

2.5.10 Detailed Phorsphoramidite Synthetic Protocols

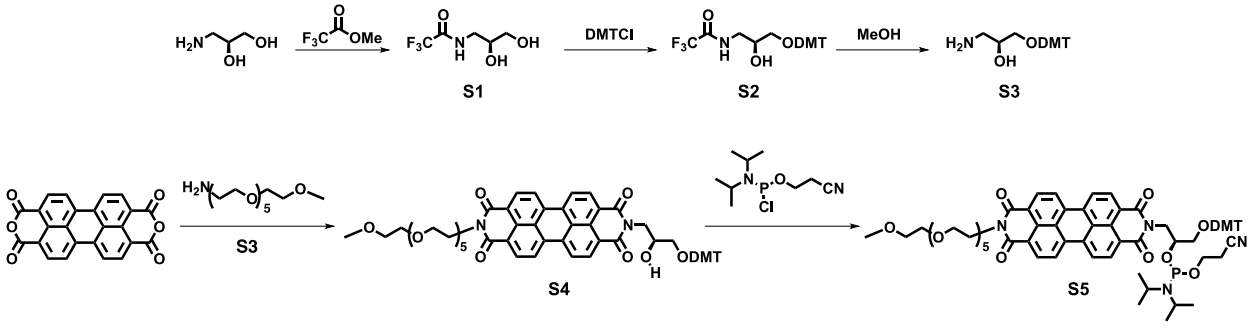

Scheme 2.1. Schematic of the synthesis of perylenediimide phosphoramidite **S5.**

A. (S)-3-trifluoroacetamido-1,2-propanediol (S1). Product **S1** in Scheme S2.1 was synthesized according to established literature protocols.[48,49] ^{1}H NMR (500 MHz, $CDCl_3$) δ 6.85 – 6.81 (br s, 1H), 3.96 – 3.88 (p, *J* = 5.8 Hz, 1H), 3.78 – 3.71 (dd, *J* = 11.2, 4.0 Hz, 1H), 3.69 – 3.56 (m, 2H), 3.46 – 3.37 (m, 1H); ^{13}C NMR (125 MHz, CD_3OD) δ 159.72 – 158.84 (q, *J* = 36.7 Hz), 120.95 – 114.11 (q, *J* = 285 Hz), 71.23, 65.12, 43.82. ^{19}F NMR (376 MHz, CD_3OD) δ –77.58; ESI MS found 210.01 and 397.06 (M + Na and 2M + Na).

B. (S)-3-trifluoroacetamido-1-(4,4'-dimethoxytriphenylmethyl)-2-propanediol (S2). Product **S2** in Scheme S2.1 was synthesized according to established literature protocols.[48,49] ^{1}H NMR (600 MHz, $CDCl_3$) δ 7.41 – 7.38 (m, 2H), 7.32 – 7.27 (m), 7.25 – 7.21 (m, 1H), 6.86 – 6.81 (m, 4H), 6.70 – 6.62 (br s), 3.94 – 3.88 (m, 1H), 3.81 – 3.77 (s, 6H), 3.63 – 3.57 (ddd, *J* = 13.9, 6.7, 3.8 Hz, 1H), 3.33 – 3.295 (dd, *J* = 7.2, 4.8 Hz), 3.295 – 3.26 (dd, *J* = 9.9, 4.5 Hz, 1H), 3.17 – 3.12 (dd, *J* = 9.7, 6.1 Hz, 1H), 2.44 – 2.41 (d, *J* = 4.6 Hz, 1H); ^{13}C NMR (126 MHz, $CDCl_3$) δ 158.87, 150.00, 144.52, 136.22, 135.61, 135.58, 130.14, 128.21, 128.14, 127.26, 123.97, 113.49, 86.84, 69.12, 64.93, 55.45, 42.78; ESI MS found 512.14 (M + Na).

C. (S)-3-amino-1-(4,4'-dimethoxytriphenylmethyl)- 2-propanediol (S3). Product **S3** in Scheme S2.1 was synthesized according to established literature protocols.[48,49] ^{1}H NMR (500 MHz, $CDCl_3$) δ 7.46 – 7.42 (m, 2H), 7.36 – 7.26 (m, 6H), 7.24 – 7.19 (tt, *J* = 7.25, 1.5 Hz, 1H), 6.86 – 6.79 (apar dt, *J* = 9, 2.75 Hz, 4H), 3.79 (s, 6H), 3.78 – 3.72 (m, 1H), 3.17 – 3.12 (d, *J* = 5.4 Hz, 2H), 2.85 – 2.80 (dd, *J* = 13.0, 4.0 Hz, 1H), 2.76 – 2.71 (dd, *J* = 13, 7.0 Hz, 1H), 1.97 (br s, 3H); ^{13}C NMR (125 MHz, $CDCl_3$) δ 158.66, 144.97, 136.13, 130.20, 128.30, 128.01, 126.98, 113.31, 86.28, 71.14, 65.67, 55.37, 44.56; ESI MS found 416.14, 787.29, and 809.29 (M + Na, 2M + 1, 2M + Na).

D. Precursor for the Perylenediimide Phosphoramidite (S4). Product **S4** in Scheme S2.1 was synthesized according to a procedure adopted from the literature.[29,30,49] First, 0.741 g (1.91 mmol, 1.0 equiv) of 3,4,9,10-perylenetetracarboxylic dianhydride and 0.713 g (3.89 mmol, 2.0 equiv) of anhydrous $Zn(OAc)_2$ were combined in an oven-dried round bottom flask. Anhydrous pyridine (17 mL) was then added via syringe, and the flask was fitted with a water-cooled condenser. The mixture was heated to reflux, and after 1.5 h, a solution of 2,5,8,11,14,17-Hexaoxanonadecan-19-amine (0.568 g, 1.92 mmol, 1.0 equiv) in 10 mL of anhydrous pyridine and a solution of (S)-3-amino-1-(4,4'-dimethoxytriphenylmethyl)-2-propanediol (0.755 g, 1.92 mmol, 1.0 equiv) in 10 mL anhydrous pyridine were successively added to the flask. The resulting mixture was stirred rapidly and maintained at reflux for ~22 hours under argon. The reaction was subsequently allowed to cool to room temperature, concentrated to ~1/10 of the original volume by rotary evaporation, diluted in CH_2Cl_2 (150 mL), and poured into a separatory funnel. The crude mixture was extracted with aqueous KOH (1 M, 3 x 150 mL), dried for 5 min over anhydrous Na_2SO_4, and filtered. Next, silica gel (8 mL) was added to the crude

product solution, and the solvent was removed by rotary evaporation. The resulting material was loaded in its dry state onto a silica gel column (245 mL silica gel, 5.5 cm O.D. column), and the products were eluted with CH_2Cl_2:methanol (from 99:1 to 85:15 in 3000 mL total eluent). The procedure yielded 820 mg (41%) of product **S4** as a dark red solid. ^{1}H NMR (500 MHz, CD_2Cl_2) δ 8.37 (dd, *J* = 18.2, 7.9 Hz, 4H), 8.16 (t, *J* = 8.5 Hz, 4H), 7.54 – 7.49 (m, 2H), 7.40 – 7.35 (m, 4H), 7.33 – 7.27 (m, 2H), 7.25 – 7.17 (m, 1H), 6.89 – 6.78 (m, 4H), 4.56 (dd, *J* = 14.4, 9.7 Hz, 1H), 4.39 (dt, *J* = 7.2, 3.7 Hz, 2H), 4.29 – 4.24 (m, 2H), 3.85 – 3.81 (m, 2H), 3.76 (d, *J* = 1.2 Hz, 6H), 3.72 – 3.67 (m, 2H), 3.62 – 3.51 (m, 16H), 3.49 – 3.46 (m, 2H), 3.31 (s, 5H), 3.18 (d, *J* = 6.5 Hz, 1H). ^{13}C NMR (126 MHz, CD_2Cl_2) δ 163.7, 163.1, 159.0, 145.5, 136.4, 133.8, 133.6, 131.0, 130.8, 130.5, 128.8, 128.7, 128.5, 128.2, 127.1, 125.4, 123.0, 113.4, 86.4, 72.2, 70.8, 70.7, 70.5, 69.6, 68.1, 66.3, 59.0, 55.6, 44.3, 39.8, 30.1. ESI MS Found 1067.36 (M + Na).

E. Perylenediimide Phosphoramidite (S5). Product **S5** in Scheme S2.1 was synthesized according to a procedure adopted from the literature.[29,30,49] First, 0.4 g (0.383 mmol, 1.0 equiv) of the perylenediimide precursor (**S4),** dichloromethane (4 mL), and distilled triethylamine (0.27 mL, 1.91 mmol, 5 equiv) were added to a scintillation vial under nitrogen. Once **S4** had dissolved to produce an opaque red solution, 0.085 mL of *N,N*-diisopropylamino-β-cyanoethyl chlorophosphoramidite (0.381 mmol, 0.99 equiv) was added *via* syringe. After stirring for 3 hours, the solution was poured into a separatory funnel, rinsed and diluted with sparged CH_2Cl_2 (3 x 4 mL), and extracted with sparged aqueous $NaHCO_3$ (saturated, 3 x 10 mL). The organic phase was dried for 1 min over Na_2SO_4, filtered, and concentrated by rotary evaporation/vacuum drying to yield 438 mg (92%) of product **S5** as a dark red solid. This product contained a mixture of

diastereomers. ^{1}H NMR (600 MHz, CD_2Cl_2) δ 8.70 – 8.34 (m, 8H), 7.61 – 7.05 (m, 9H), 6.86 – 6.67 (m, 4H), 4.67 – 4.50 (m, 1H), 4.45 – 4.39 (m, 2H), 4.36 – 4.21 (m, 1H), 3.82 (t, *J* = 6.5 Hz, 2H), 3.75 (d, *J* = 2.3 Hz, 1H), 3.73 (s, 2H), 3.70 (d, *J* = 5.0 Hz, 3H), 3.69 – 3.65 (m, 3H), 3.65 (s, 2H), 3.61 – 3.46 (m, 21H), 3.32 (d, *J* = 1.6 Hz, 3H), 3.24 – 3.02 (m, 1H), 2.42 (td, *J* = 6.7, 3.7 Hz, 1H), 2.33 (t, *J* = 6.6 Hz, 1H), 1.05 (dd, *J* = 11.9, 6.8 Hz, 6H), 0.98 (dd, *J* = 12.9, 6.8 Hz, 6H). ^{13}C NMR (126 MHz, CD_2Cl_2) δ 163.7, 163.6, 163.6, 159.1, 159.0, 159.0, 158.9, 145.6, 145.5, 136.7, 136.6, 136.4, 136.4, 134.7, 134.6, 134.6, 134.4, 131.5, 131.3, 130.7, 130.5, 130.5, 129.5, 129.5, 128.7, 128.4, 128.3, 128.2, 127.1, 126.6, 126.5, 123.7, 123.6, 123.5, 123.5, 123.4, 123.3, 118.3, 118.1, 113.6, 113.5, 113.5, 113.4, 113.4, 86.7, 86.7, 72.4, 71.2, 71.1, 71.0, 70.9, 70.8, 70.2, 68.4, 66.2, 59.2, 59.0, 58.9, 58.8, 58.6, 55.7, 55.7, 55.6, 55.6, 45.8, 45.8, 43.7, 43.6, 43.5, 43.4, 39.9, 24.9, 24.8, 24.8, 24.7, 24.7, 23.2, 23.2, 20.7, 20.6, 20.5, 20.4. ^{31}P NMR (243 MHz, CD_2Cl_2) δ 149.7 (d, *J* = 15.9 Hz). ESI MS Found 1267.52 (M + Na).

2.5.11 Supporting Figures

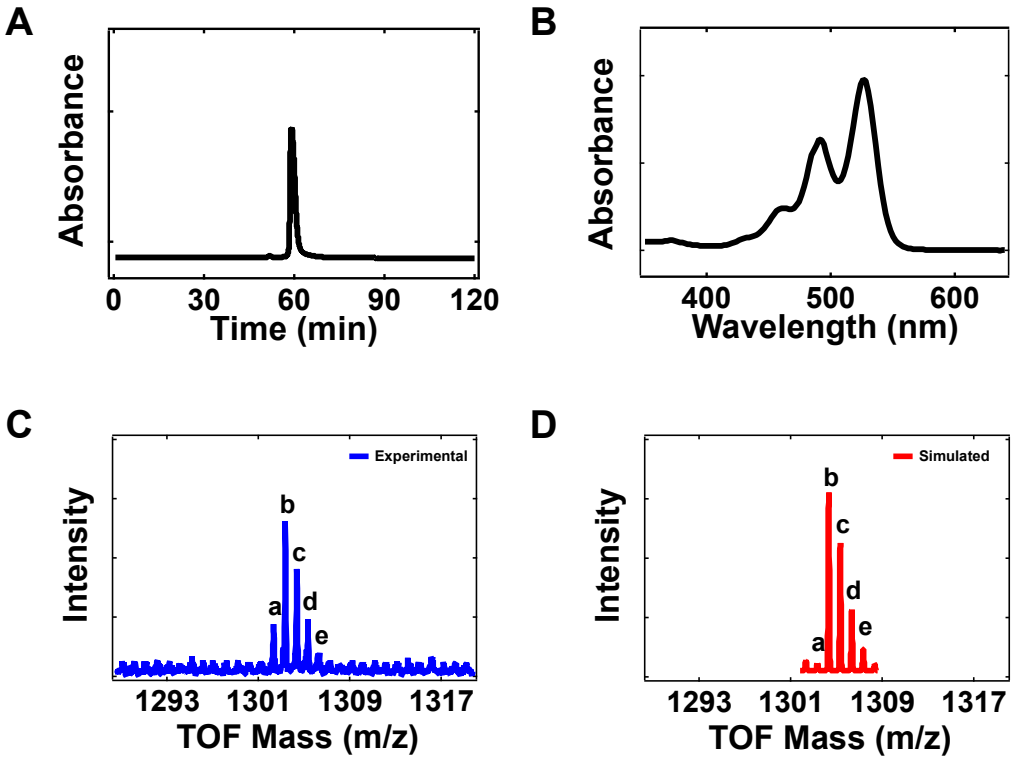

Figure S2.1: (A) Typical HPLC chromatogram corresponding to the purification of **P1**. Note the presence of a single main peak. (B) The corresponding normalized UV-Vis absorbance spectrum for **P1**. (C) Typical experimental MALDI-TOF spectrum for **P1**. (D) Simulated MALDI-TOF spectrum for **P1**. The peaks in the experimental and simulated traces that correspond to one another are labeled with the same letter. Note that the observed and expected masses are in good agreement.

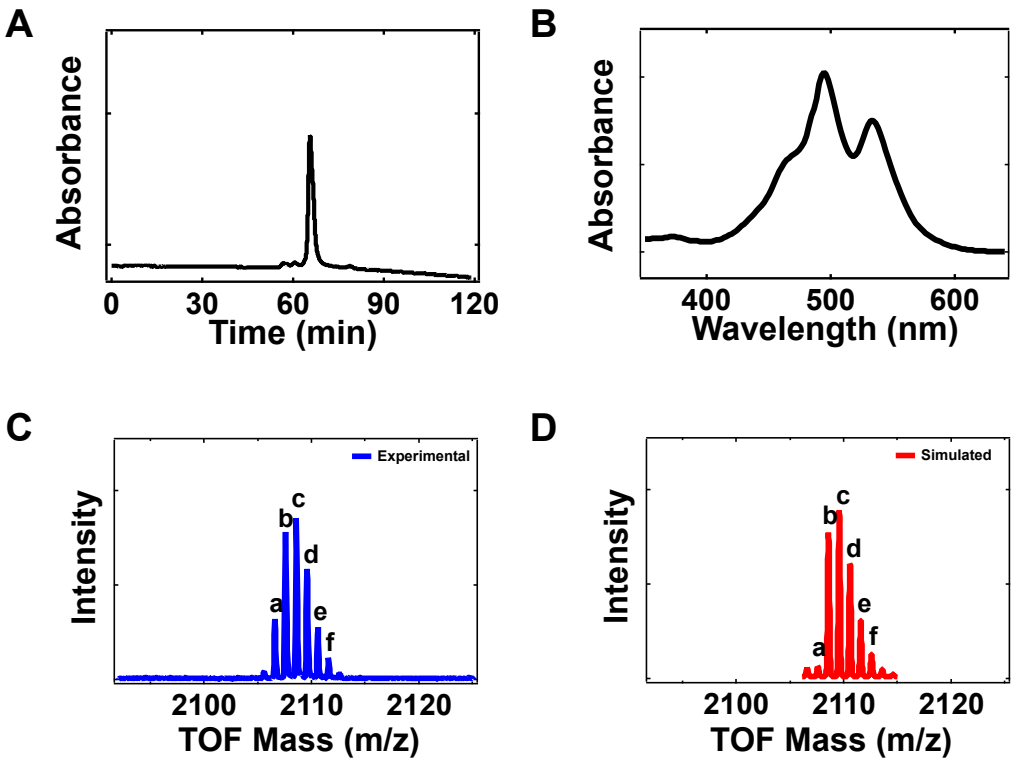

Figure S2.2: (A) Typical HPLC chromatogram corresponding to the purification of **P2**. Note the presence of a single main peak. (B) The corresponding normalized UV-Vis absorbance spectrum for **P2**. (C) Typical experimental MALDI-TOF spectrum for **P2**. (D) Simulated MALDI-TOF spectrum for **P2**. The peaks in the experimental and simulated traces that correspond to one another are labeled with the same letter. Note that the observed and expected masses are in good agreement.

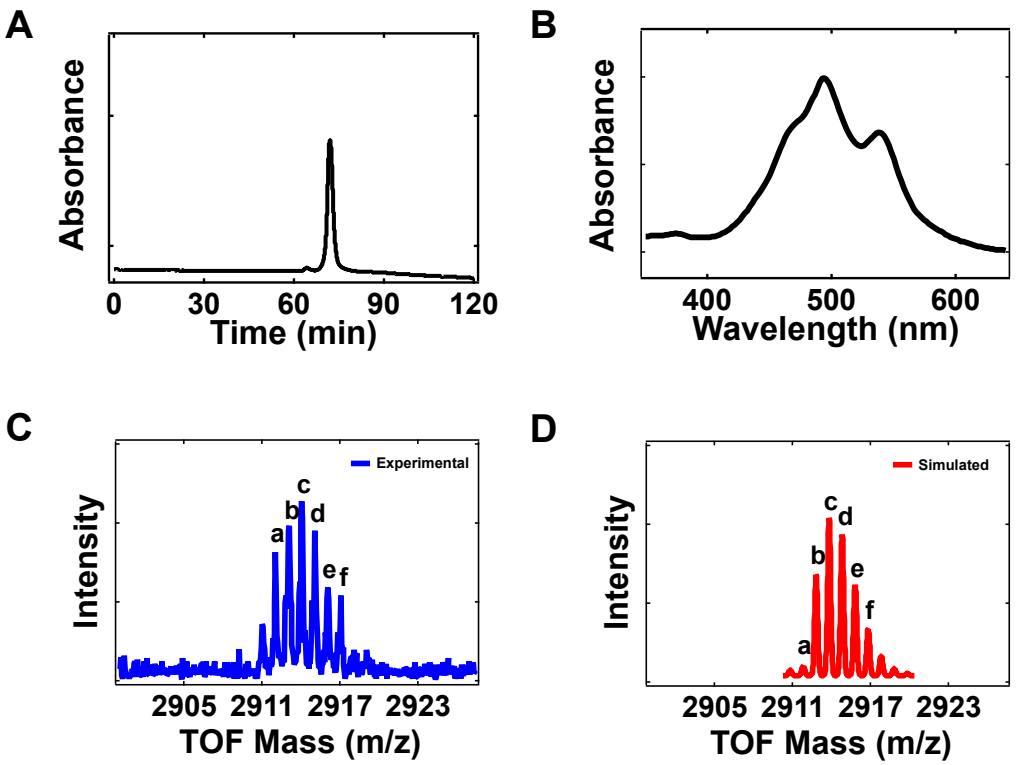

Figure S2.3: (A) Typical HPLC chromatogram corresponding to the purification of **P3**. Note the presence of a single main peak. (B) The corresponding normalized UV-Vis absorbance spectrum for **P3**. (C) Typical experimental MALDI-TOF spectrum for **P3**. (D) Simulated MALDI-TOF spectrum for **P3**. The peaks in the experimental and simulated traces that correspond to one another are labeled with the same letter. Note that the observed and expected masses are in good agreement.

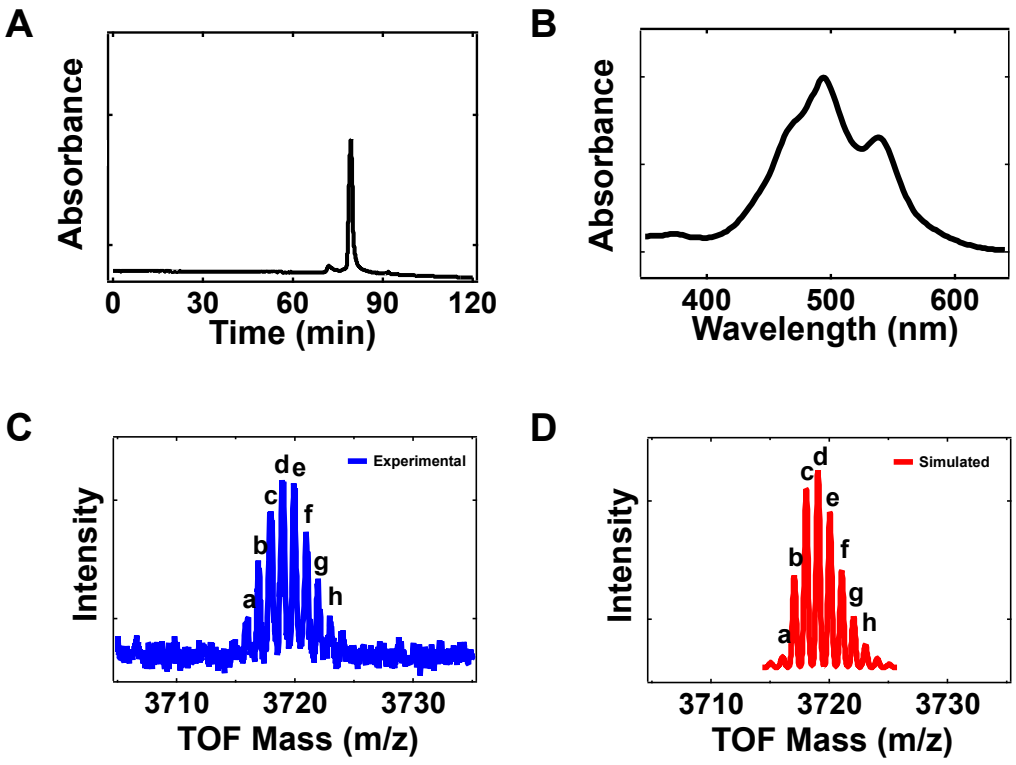

Figure S2.4: (A) Typical HPLC chromatogram corresponding to the purification of **P4**. Note the presence of a single main peak. (B) The corresponding normalized UV-Vis absorbance spectrum for **P4**. (C) Typical experimental MALDI-TOF spectrum for **P4**. (D) Simulated MALDI-TOF spectrum for **P4**. The peaks in the experimental and simulated traces that correspond to one another are labeled with the same letter. Note that the observed and expected masses are in good agreement.

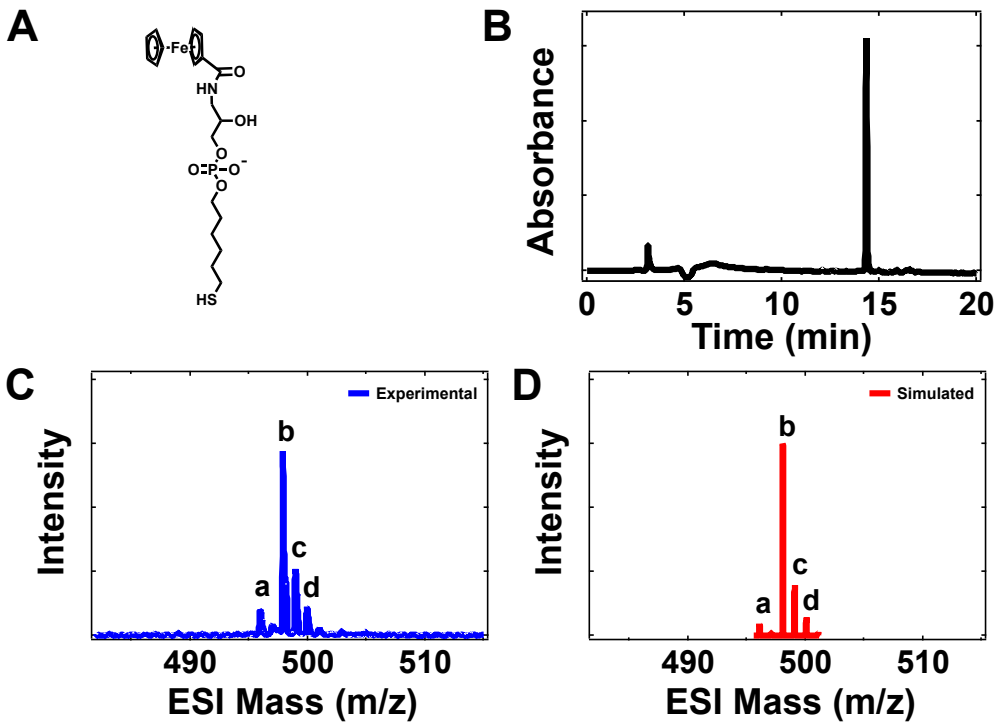

Figure S2.5: (A) Chemical structure of **P0**. (B) Typical HPLC chromatogram corresponding to the purification of **P0**. (C) Typical experimental ESI$^-$ spectrum for **P0**. (D) Simulated ESI$^-$ spectrum for **P0**. The peaks in the experimental and simulated traces that correspond to one another are labeled with the same letter. Note that the observed and expected masses are in good agreement.

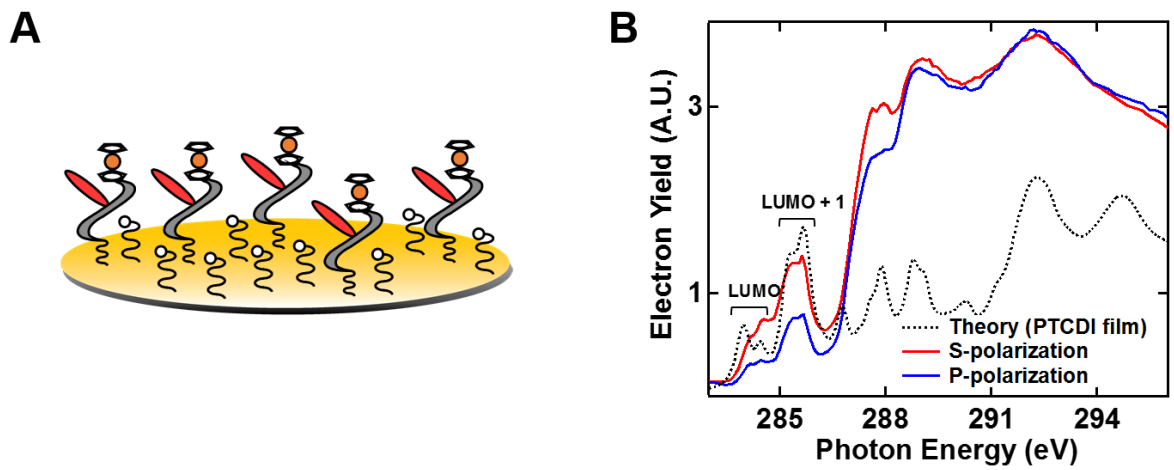

Figure S2.6: (A) Schematic of a mercaptohexanol-backfilled monolayer from **P1**. (B) Carbon K-edge NEXAFS spectra of the **P1** monolayer measured with the electric field polarized parallel (red) and perpendicular (blue) to the gold surface. The predicted theoretical spectrum for PTCDI is shown for comparison (dashed trace). The substrate-relative orientation reported for the PTCDIs within the monolayer was calculated from the difference in signal intensity (dichroism) between the red and blue traces.

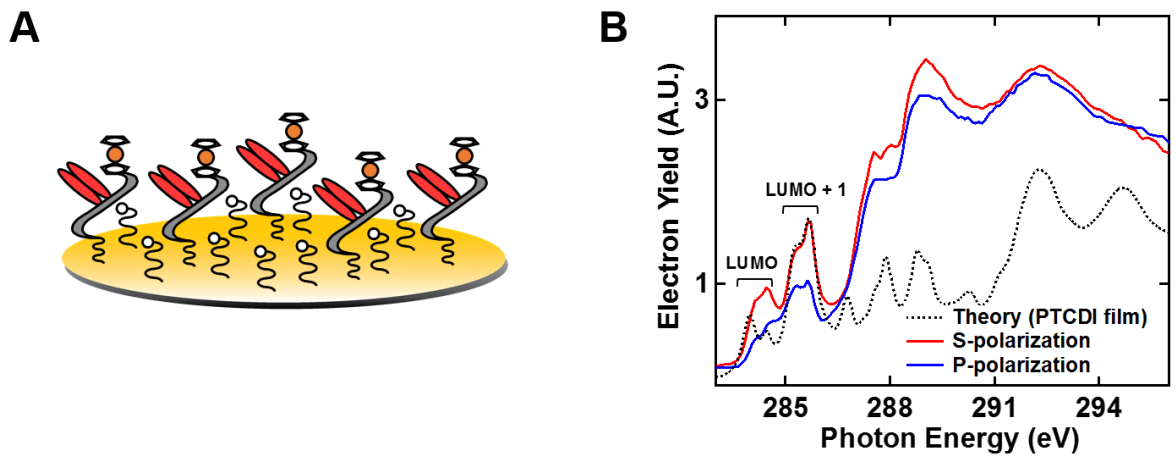

Figure S2.7: (A) Schematic of a mercaptohexanol-backfilled monolayer from **P2**. (B) Carbon K-edge NEXAFS spectra of the **P2** monolayer measured with the electric field polarized parallel (red) and perpendicular (blue) to the gold surface. The predicted theoretical spectrum for PTCDI is shown for comparison (dashed trace). The substrate-relative orientation reported for the PTCDIs within the monolayer was calculated from the difference in signal intensity (dichroism) between the red and blue traces.

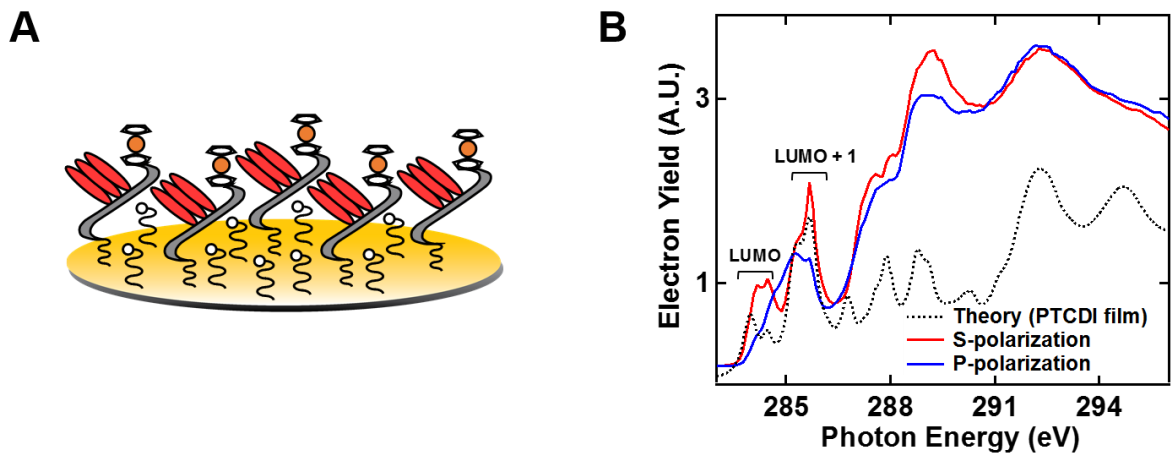

Figure S2.8: (A) Schematic of a mercaptohexanol-backfilled monolayer from **P3**. (B) Carbon K-edge NEXAFS spectra of the **P3** monolayer measured with the electric field polarized parallel (red) and perpendicular (blue) to the gold surface. The predicted theoretical spectrum for PTCDI is shown for comparison (dashed trace). The substrate-relative orientation reported for the PTCDIs within the monolayer was calculated from the difference in signal intensity (dichroism) between the red and blue traces.

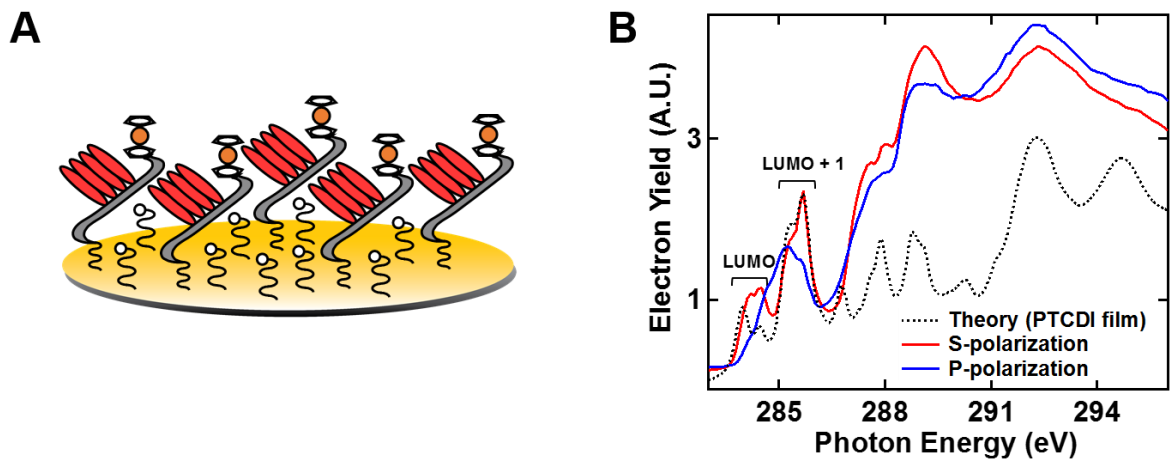

Figure S2.9: (A) Schematic of a mercaptohexanol-backfilled monolayer from **P4**. (B) Carbon K-edge NEXAFS spectra of the **P4** monolayer measured with the electric field polarized parallel (red) and perpendicular (blue) to the gold surface. The predicted theoretical spectrum for PTCDI is shown for comparison (dashed trace). The substrate-relative orientation reported for the PTCDIs within the monolayer was calculated from the difference in signal intensity (dichroism) between the red and blue traces.

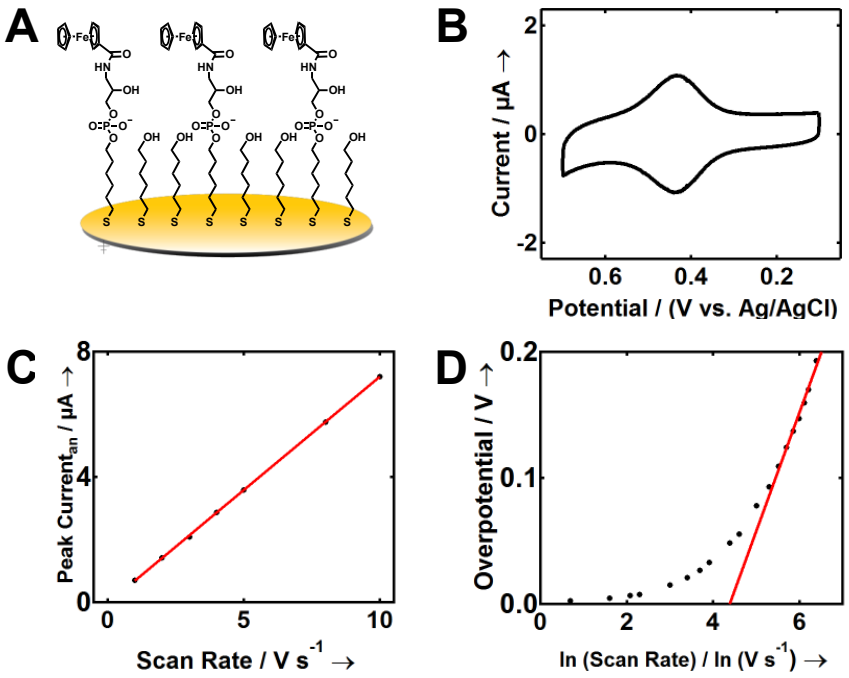

Figure S2.10: (A) Schematic of a mercaptohexanol-backfilled monolayer from **P0**. (B) Representative cyclic voltammogram obtained for a backfilled monolayer from **P0**. (C) Representative plot of the anodic peak current as a function of scan rate for a backfilled monolayer from **P0**. (D) A representative plot of the anodic overpotential as a function of the natural logarithm of the scan rate for **P0**. The red line corresponds to the linear fit of the region with η > 100 mV, which is used to obtain the electron transfer coefficient α and the standard electron transfer rate constant k_0.

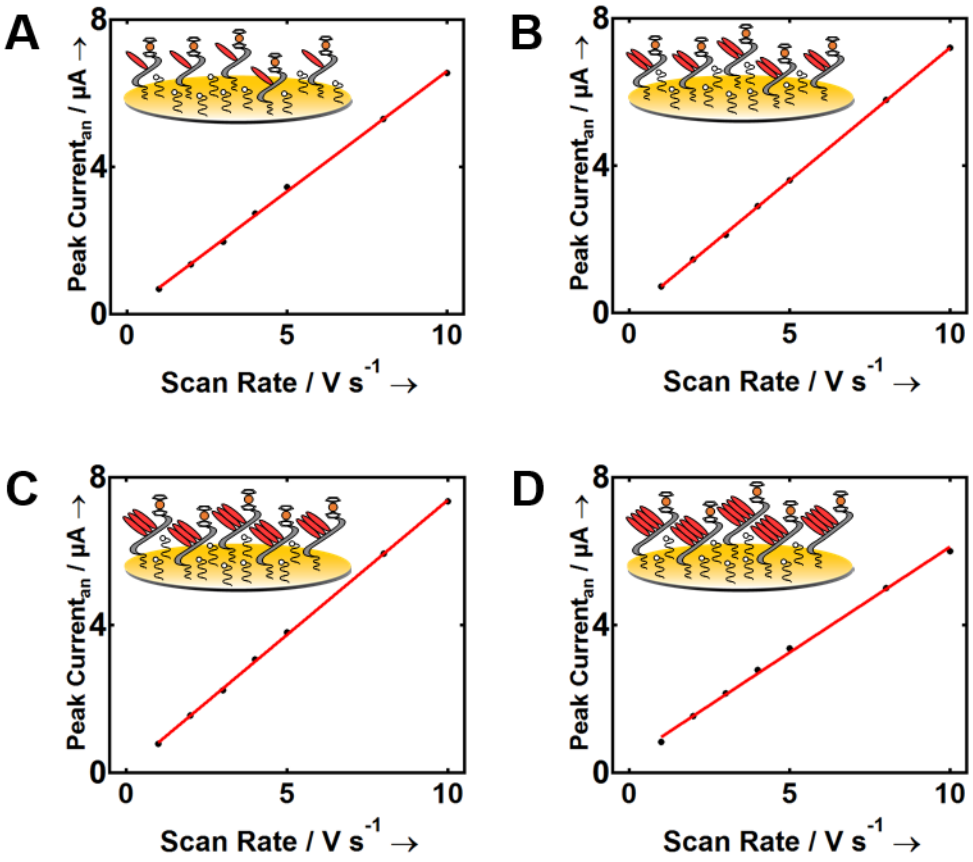

Figure S2.11: The dependence of the anodic peak current on the scan rate for monolayers from (A) **P1, (**B) **P2**, (C) **P3**, and (D) **P4**. The insets are schematics of the corresponding monolayers. Note that the linear dependence is indicative of a surface-bound species.

Monolayer Feature	P0	P1	P2	P3	P4
Midpoint Potential (V)	0.46 (0.02)	0.52 (0.02)	0.52 (0.04)	0.47 (0.03)	0.48 (0.002)
Peak Current Ratio	1.07 (0.04)	1.02 (0.03)	1.06 (0.04)	1.10 (0.06)	1.16 (0.03)
$FWHM_a$ (V)	0.14 (0.004)	0.13 (0.006)	0.13 (0.003)	0.13 (0.005)	0.13 (0.003)
Surface Coverage (pmol cm^{-2})	22.2 (4.3)	24.1 (5.1)	24.9 (4.2)	20.2 (2.5)	20.1 (3.0)

Table S2.1: Tabulated midpoint potentials, anodic to cathodic peak current ratios, anodic peak full widths at half maximum, and average surface coverages for **P0**, **P1**, **P2**, **P3**, and **P4**. The measurements correspond to a minimum of five independent electrodes, with the standard deviations noted in parentheses.

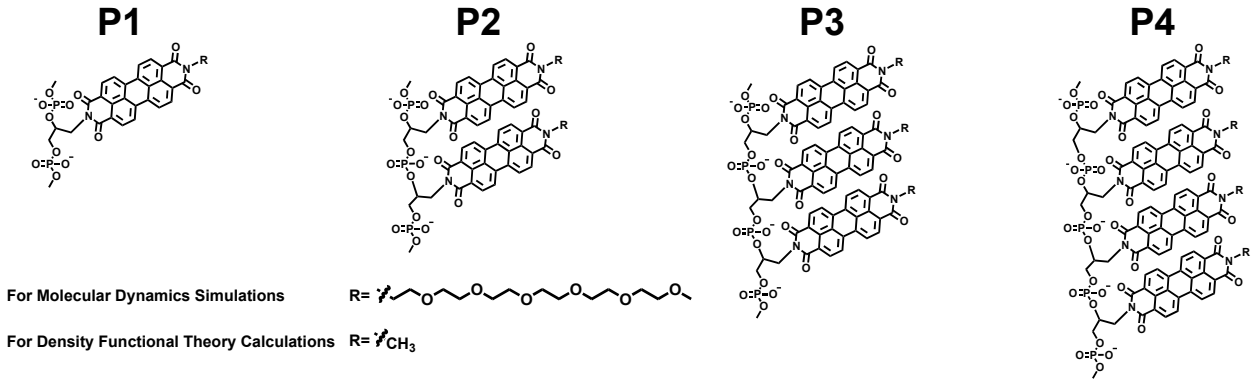

Figure S2.12: The chemical structures of the PTCDI-based substructures used for the molecular dynamics simulations and density functional theory calculations.

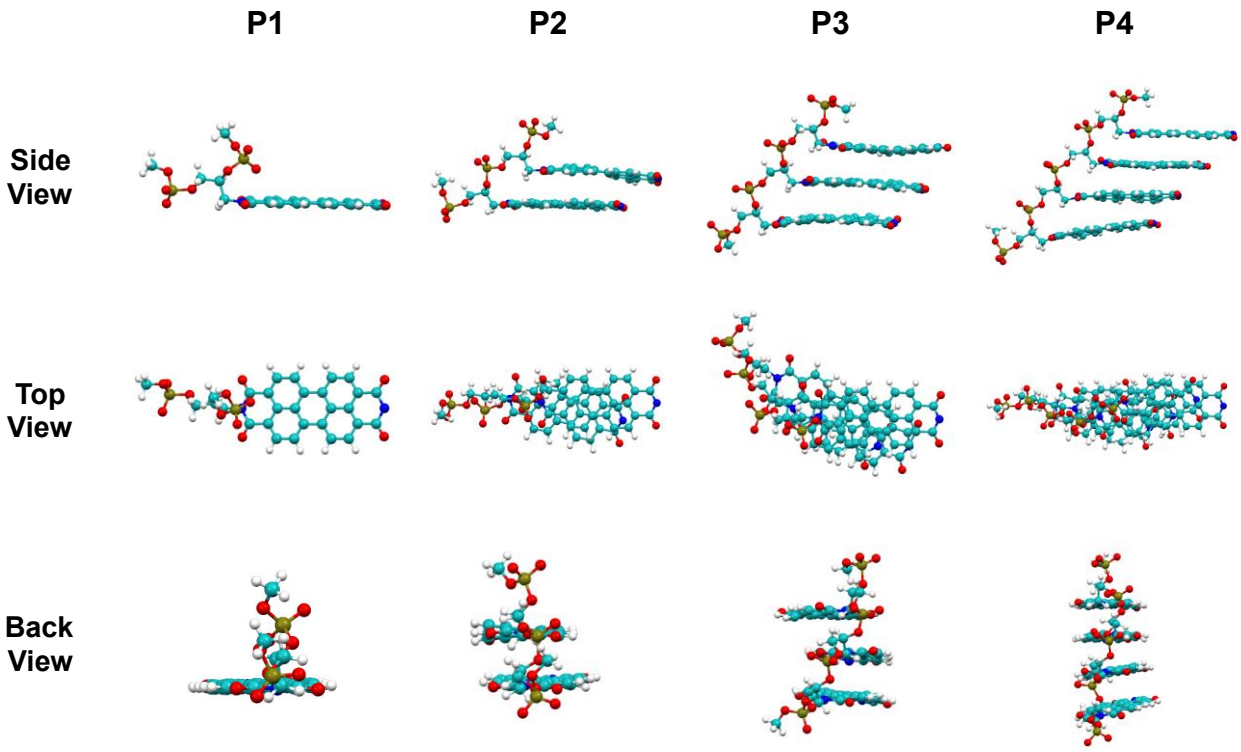

Figure S2.13: Side, top, and back views of the equilibrium conformations of the PTCDI-containing substructures of **P1**, **P2**, **P3**, and **P4**, as obtained from the molecular dynamics simulations.

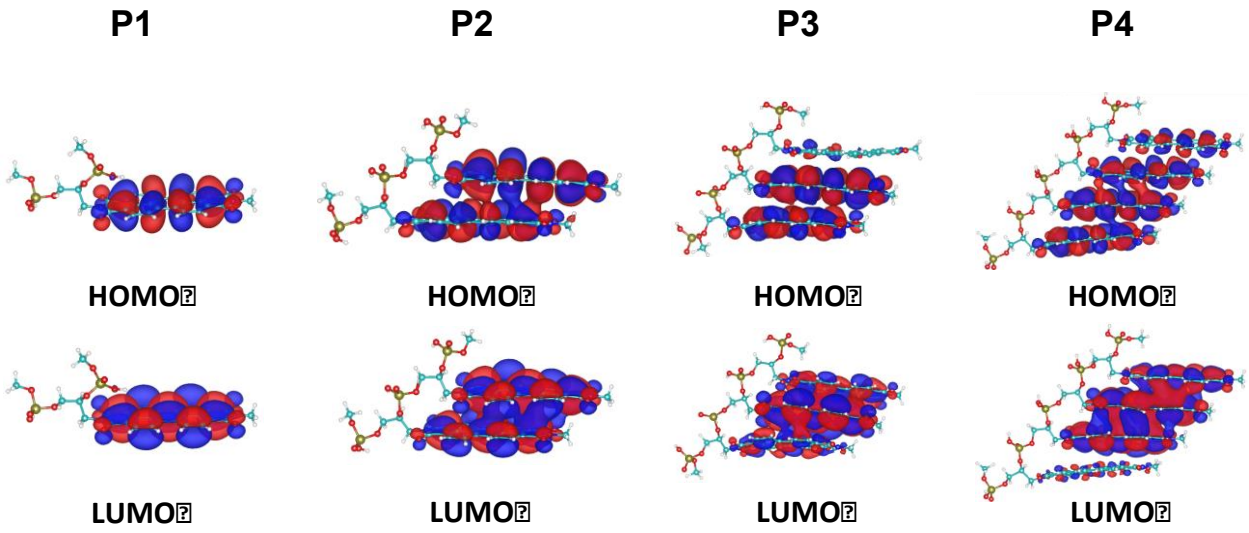

Figure S2.14: Isosurface plots for the HOMO and LUMO of **P1**, **P2**, **P3**, and **P4**. The isosurface values for all of the plots have been set to 0.01 |e|/Å^3.

2.6 References

[1] K. Moth-Poulsen, *Handbook of Single-Molecule Electronics*, Pan Stanford Publishing, Boca Raton, **2015**.

[2] D. M. Guldi, H. Nishihara, L. Venkataraman, *Chem. Soc. Rev.* **2015**, *44*, 842–844.

[3] M. U. Winters, E. Dahlstedt, H. E. Blades, C. J. Wilson, M. J. Frampton, H. L. Anderson, B. Albinsson, *J. Am. Chem. Soc.* **2007**, *129,* 4291–4297.

[4] G. Sedghi, V. M. García-Suárez, L. J. Esdaile, H. L. Anderson, C. J. Lambert, S. Martín, D. Bethell, S. J. Higgins, M. Elliot, N. Bennett, J. E. Macdonald, R. J. Nichols, *Nat. Nanotech.* **2011**, *6*, 517–523.

[5] G. Sedghi, L. J. Esdaile, H. L. Anderson, S. Martin, D. Bethell, S. J. Higgins, R. J Nichols, *Adv. Mater.* **2012**, *24*, 653–657.

[6] W. B. Davis, W. A. Svec, M. A. Ratner, M. R. Wasielewski, *Nature* **1998**, *396*, 60–63.

[7] H. D. Sikes, J. F. Smalley, S. P. Dudek, A. R. Cook, M. D. Newton, C. E. D. Chidsey, S. W. Feldburg, *Science* **2001**, *291*, 1519–1523.

[8] F. Giacalone, J. L. Segura, N. Martín, D. M. Guldi, *J. Am. Chem. Soc.* **2004**, *126*, 5340–5341.

[9] S. O. Kelley, N. M. Jackson, M. G. Hill, J. K. Barton, *Angew. Chem. Int. Ed.* **1999**, *38*, 941–945; *Angew. Chem.* **1999**, *111*, 991–996.

[10] J. D. Slinker, N. B. Muren, S. E. Renfrew, J. K. Barton, *Nat. Chem.* **2011**, *3*, 228–233.

[11] L. Xiang, J. L. Palma, C. Bruot, V. Mujica, M. A. Ratner, N. Tao, *Nat. Chem.* **2015**, *7*, 221–226.

[12] N. J. Tao, *Nat. Nanotech.* **2006**, *1*, 173–181.
[13] S. V. Aradhya, L. Venkataraman, *Nature Nanotech.* **2013**, *8*, 399–410.
[14] C. Jia, B. Ma, N. Xin, X. Guo, *Acc. Chem. Res.* **2015**, *48*, 2565–2575.
[15] H. Song, M. A. Reed, T. Lee, *Adv. Mater.* **2011**, *23*, 1583–1608.
[16] M. D. Newton, J. F. Smalley, *Phys. Chem. Chem. Phys.* **2007**, *9*, 555–572.
[17] A. L. Eckermann, D. J. Field, J. A. Shaw, T. J. Meade, *Coord. Chem. Rev.* **2010**, *254*, 1769–1802.
[18] E. A. Weiss, M. R. Wasielewski, M. A. Ratner, *Top. Curr. Chem.* **2005**, *257*, 103–133.
[19] C. Schubert, J. T. Margraf, T. Clark, D. M. Guldi, *Chem. Soc. Rev.* **2015**, *44*, 988–998.
[20] S. S. Skourtis, *Biopolymers*, **2013**, *100*, 82–92.
[21] R. J. Nichols, S. J. Higgins, *Annu. Rev. Anal. Chem.* **2015**, *8*, 389-417.
[22] "IBM Announces $3 Billion Research Initiative to Tackle Chip Grand Challenges for Cloud and Big Data Systems", can be found under http://www-03.ibm.com/press/us/en/pressrelease/44357.wss#release
[23] C. Huang, S. Barlow, S. R. Marder, *J. Org. Chem.* **2011**, *76*, 2386–2407.
[24] F. Würthner, *Chem. Commun.* **2004**, 1564–1579.
[25] C. Wagner, H.-A. Wagenknecht, *Org. Lett.* **2006**, *8*, 4191–4194.
[26] D. Baumstark, H.-A. Wagenknecht, *Chem. Eur. J.* **2008**, *14*, 6640 – 6645.
[27] T. A. Zeidan, R. Carmieli, R. F. Kelley, T. M. Wilson, F. D. Lewis, M. R. Wasielewski, *J. Am. Chem. Soc.* **2008**, *130*, 13945–13955.
[28] T. M. Wilson, T. A. Zeidan, M. Hariharan, F. D. Lewis, M. R. Wasielewski, *Angew. Chem. Int. Ed.* **2010**, *49*, 2385–2388; *Angew. Chem.* **2010**, *122*, 2435–2438.
[29] C. H. Wohlgamuth, M. A. McWilliams, A. Mazaheripour, A. M. Burke, K.-Y. Lin, L. Doan, J. D. Slinker, A. A. Gorodetsky, *J. Phys. Chem. C* **2014**, *118*, 29084–29090.
[30] C. B. Markegard, A. Mazaheripour, J.-M. Jocson, A. M. Burke, M. N. Dickson, A. A. Gorodetsky, H. D. Nguyen, *J. Phys. Chem. B* **2015**, *119*, 11459–11465.
[31] J. C. Love, L. A. Estroff, J. K. Kriebel, R. G. Nuzzo, G. M. Whitesides, *Chem. Rev.* **2005**, *105*, 1103–1169.
[32] K. J. Odenthal, J. J. Gooding, *Analyst*, **2007**, *132*, 603–610.
[33] A. A. Gorodetsky, M. C. Buzzeo, J. K. Barton, *Bioconjugate Chem.* **2008**, *19*, 2285–2296.
[34] J. Stöhr, *NEXAFS Spectroscopy*, Springer-Verlag, Berlin/Heidelberg, Germany, **1992**.
[35] G. Fratesi, V. Lanzilotto, S. Stranges, M. Alagia, G. P. Brivio, L. Floreano, *Phys. Chem. Chem. Phys.* **2014**, *16*, 14834–2296.
[36] D. B. Robinson, C. E. D. Chidsey, *J. Phys. Chem. B*, **2002**, *106*, 10706–10713.
[37] K. Weber, L. Hockett, S. Creager, *J. Phys. Chem. B* **1997**, *101*, 8286–8291.
[38] J. F. Smalley, H. O. Finklea, C. E. D. Chidsey, M. R. Linford, S. E. Creager, J. P. Ferraris, K. Chalfant, T. Zawodzinsk, S. W. Feldberg, M. D. Newton, *J. Am. Chem. Soc.* **2003**, *125*, 2004–2013.
[39] A. J. Bard, L. R. Faulkner, *Electrochemical Methods: Fundamentals and Applications*, 2nd ed., Wiley, New York, **2000**.
[40] R. C. Mucic, M. K. Herrlein, C. A. Mirkin, R. L. Letsinger, *Chem. Commun.* **1996**, 555–557.
[41] C. E. D. Chidsey, C. R. Bertozzi, T. M. Putvinski, A. M. Mujsce, *J. Am. Chem. Soc.* **1990**, *112*, 4301–4306.
[42] E. Laviron, *J. Electroanal. Chem.* **1979**, *101*, 19–28.

[43] T. Yanai, D. P. Tew, N. C. Handy, *Chem. Phys. Lett*. **2004**, *393*, 51–57.
[44] A. Mazaheripour, G. Kladnik, J.-M. Jocson, A. G. Wardrip, C. B. Markegard, N. Frey, A. Cossaro, L. Floreano, A. Verdini, A. Bartlett, A. M. Burke, N. Hüsken, K. Miller, K. Van Wonterghem, R. Lopez, M. Lu, A. Masurkar, M. N. Dickson, S. Sharifzadeh, H. Nguyen, I. Kymissis, D. Cvetko, A. Morgante, A. A. Gorodetsky. *Mater. Horiz.* **2017**, *4*, 437–441.
[45] R. K. Harris, E. D. Becker, S. M. Cabral de Menezes, P. Granger, R. E. Hoffman, K. W. Zilm, *Pure Appl. Chem.* **2008**, *80,* 59–84.
[46] N. Hüsken, M. Gębala, F. La Mantia, W. Schuhmann, N. Metzler-Nolte, *Chem. Eur. J.* **2011**, *17*, 9678–9690.
[47] L. Floreano, G. Naletto, D. Cvetko, R. Gotter, M. Malvezzi, L. Marassi, A. Morgante, A. Santaniello, A. Verdini, F. Tommasini, G. Tondello, *Rev. Sci. Instrum.* **1999**, *70*, 3855–3864.
[48] L. Floreano, A. Cossaro, R. Gotter, A. Verdini, G. Bavdek, F. Evangelista, A. Ruocco, A. Morgante, D. Cvetko, *J. Phys. Chem. C* **2008**, *112*, 10794–10802.
[49] P. Vilmercati, D. Cvetko, A. Cossaro, A. Morgante, *Surf. Sci.* **2009**, *603*, 1542–1556.
[50] A. Batra, G. Kladnik, H. Vázquez, J. S. Meisner, L. Floreano, C. Nuckolls, D. Cvetko, A. Morgante, L. Venkataraman, *Nat. Comm.* **2012**, *3*, 1038.
[51] T. Schiros, G. Kladnik, D. Prezzi, A. Ferretti, G. Olivieri, A. Cossaro, L. Floreano, A. Verdini, C. Schenck, M. Cox, A. A. Gorodetsky, K. Plunkett, D. Delongchamp, C. Nuckolls, A. Morgante, D. Cvetko, I. Kymissis*, Adv. Energy Mater.* **2013**, *3*, 894–902.
[52] G. Fratesi *et al.*, *Phys. Chem. Chem. Phys.* **2014**, *16*, 14834–14844.
[53] Gaussian 09, Revision D.01, M. J. Frisch *et al.,* Gaussian, Inc., Wallingford CT, 2009
[54] K. Momma, F. Izumi, *J. Appl. Crystallogr.* **2011**, *44*, 1272–1276.
[55] A. V. Azhayev, M. L. Antopolsky, *Tetrahedron* **2001**, *57*, 4977–4986.

CHAPTER 3 Unexpected Length Dependence of Excited-State Charge Transfer Dynamics for Surface-Confined Perylenediimide Ensembles

3.1 Abstract

The performance of devices from organic semiconductors is often governed by charge transfer phenomena at structurally and electronically complex interfaces, which remain challenging to access and study with excellent chemical and temporal resolution. Herein, we report the preparation and X-ray spectroscopic characterization of well-defined model organic-inorganic interfaces. We discover an unexpected trend for our systems' associated charge transfer times, and we rationalize this trend with density functional theory calculations. Our findings hold relevance for understanding interfacial charge transfer phenomena in a variety of organic, biological, and bioinspired systems.

3.2 Introduction

Organic semiconductors have been touted as the next generation of electronic materials, with the potential to replace their more established inorganic counterparts in many devices, and as such, they have witnessed tremendous advances within the past two decades.[1-9] The performance of organic electronic devices, such as light emitting diodes, photovoltaics, and transistors, has been shown to critically depend on charge transfer phenomena at their organic-inorganic interfaces.[10-13] Traditionally, such phenomena have been studied with various spectroscopic techniques for isolated macromolecular systems in solution or thin films at solid substrates.[14-22] However, these experiments may not always adequately capture charge transfer dynamics at organic-inorganic interfaces, where molecule-molecule and molecule-substrate interactions become notoriously complicated.[10-

[13,23] Moreover, the experiments can often furnish inconclusive results at length scales of < ~ 5 nm, where the electronic structure of organic semiconductors transitions from resembling isolated molecules to resembling extended solids.[24-26] Consequently, there exists an opportunity for the development of methodologies that facilitate detailed studies of excited-state charge transfer within structurally and electronically well-defined model systems at solid substrates.

Herein, we use synchrotron-based X-ray spectroscopy to quantify excited-state charge transfer dynamics at model organic-inorganic interfaces. First, we form a series of well-defined, backfilled monolayers *via* self-assembly of distinct DNA-like macromolecules from perylene-3,4,9,10 tetracarboxylic diimide (PTCDI)[27-31] building blocks. We next probe our monolayers with resonant photoemission spectroscopy (RPES)[21,22,32-41] and use the core-hole clock (CHC)[21,22,32-41] method to quantify the rate of excited-state charge transfer, i.e. electron delocalization, from the molecules to their surroundings. We observe an unexpected length-dependent trend for the charge transfer times, which we rationalize with density functional theory calculations. Our findings hold significance for the engineering of improved interfaces in organic electronic devices and for the study of charge transfer phenomena in a variety of organic, biological, and bioinspired systems.

3.3 Results and Discussion

For our experiments, we prepared the model organic-inorganic interfaces illustrated in Figure 3.1, which drew inspiration from the architecture of organic semiconductor thin films and the self-assembly properties of duplex DNA. First, we chose the classic PTCDI organic semiconductor for our experiments because this molecule's

electronic properties and self-assembly characteristics have been extensively explored.[27-31] Next, we used established automated oligonucleotide chemistry to synthesize and characterize a series of DNA-like macromolecules (denoted as **P1**, **P2**, **P3**, and **P4**), which consisted of one to four PTCDI moieties arranged on a phospho-alkane backbone, as well as alkanethiol and ferrocene functionalities at opposing termini (Supporting Information Figures S2.1 – S2.4).[42-52] Here, the incorporation of a negatively-charged backbone and solubilizing hexaethylene glycol imide substituents facilitated processing and mitigated the possibility of intermolecular aggregation.[30,31] Subsequently, we leveraged standard DNA and alkanethiol self-assembly strategies[53-56] to form backfilled monolayers on gold substrates from our thiol-modified macromolecules. Importantly, the monolayers were relatively dilute with surface coverages of ~ 20 to ~ 25 pmol/cm^2, as determined from electrochemical measurements,[57] and their constituent PTCDI-based macromolecules adopted upright orientations at nearly identical angles of ~ 60 to ~ 61° relative to the substrates, as determined from near-edge X-ray fine structure absorption spectroscopy.[57] These precisely-defined organic-inorganic interfaces enabled the systematic investigation and direct comparison of excited-state charge transfer phenomena within a uniform context.

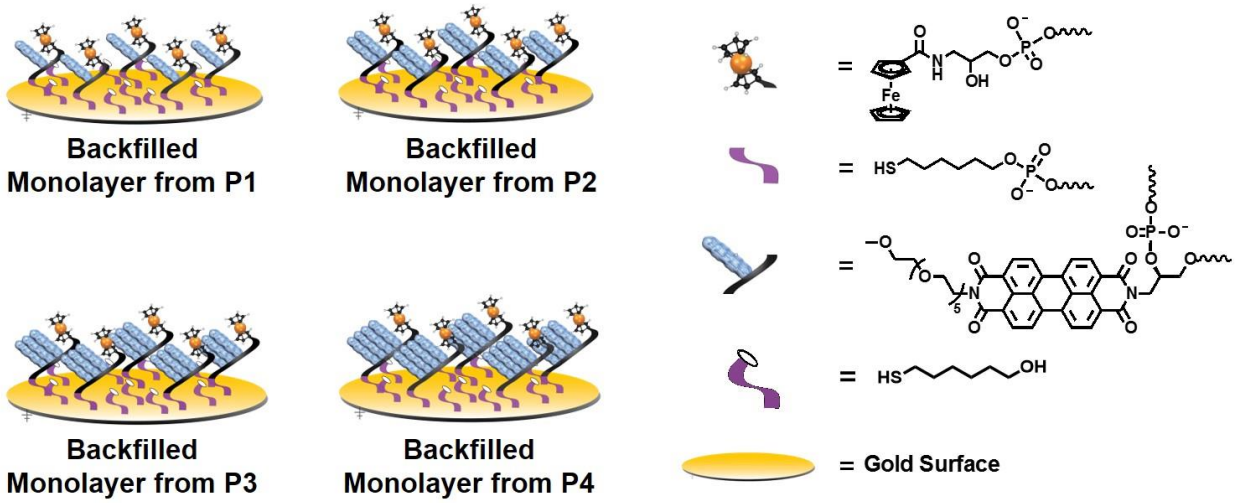

Figure 3.1: Illustration of backfilled monolayers from macromolecules **P1**, **P2**, **P3**, and **P4** on gold substrates. The macromolecules feature tracts of one, two, three, or four PTCDIs arranged on a phospho-alkane backbone, as well as terminal thiol and ferrocene moieties. The legend on the right shows the components of our model systems.

We proceeded to study charge transfer dynamics at our model organic-inorganic interfaces with synchrotron-based resonant photoemission spectroscopy (RPES), a surface-sensitive technique that provides information on interfacial charge transfer with atomic-level chemical resolution and femtosecond (or even sub-femtosecond) temporal resolution.[21,22,32-34] In a typical generalized incarnation of this technique, X-ray radiation promotes an atomically localized core electron to an unoccupied orbital (e.g, the LUMO), producing an excited electron and a core-hole (Figure 3.2A, left). Subsequently, the excited electron may relax *via* multiple pathways, including an autoionization process known as participator decay (Figure 3.2A, middle) and general charge transfer into the surroundings (Figure 3.2A, right).[21,22,32-34] For the participator decay process, the excited electron participates in the core-hole decay and another electron from an occupied orbital (e.g. the

HOMO) is ejected (Figure 3.2A, middle), yielding a resonantly enhanced peak that is degenerate with direct photoemission.[21,22,32-34] For the charge transfer process, the core-excited electron delocalizes from the macromolecules' higher-energy orbital into the substrate or general surrounding electronic environment (Figure 3.2A, right), quenching the intensity of the participator decay signal.[21,22,32-34] As a specific example, Figure 3.2B shows a two-dimensional plot of the normalized resonant photoemission intensity versus the photon energy and electron binding energy for a monolayer from **P1**, with the non-resonant background subtracted (a wider photon energy range is shown in Figure S3.1). The plot displayed a prominent peak for photon energies between 284 eV and 286 eV and binding energies between 2.2 eV to 5 eV, along with a broad Auger decay hump at higher binding energies (Figures 3.2B and S3.1). Based on the NEXAFS and RPES spectra previously reported for perylene derivatives, we attributed the prominent peak to the resonantly enhanced HOMO resulting from participator decay of a carbon 1s core electron that had been promoted to the LUMO and/or LUMO+1.[38,41,57-59] Importantly, an analysis of the spectra obtained for monolayers from **P2**, **P3**, and **P4** yielded very similar characteristic signals, which we assigned in analogous fashion (Figures S3.2-S3.3.4). These findings demonstrated that the RPES spectra of monolayers from **P1**, **P2**, **P3**, and **P4** generally resembled both one another and the spectra previously reported for various perylene derivatives.[38,41]

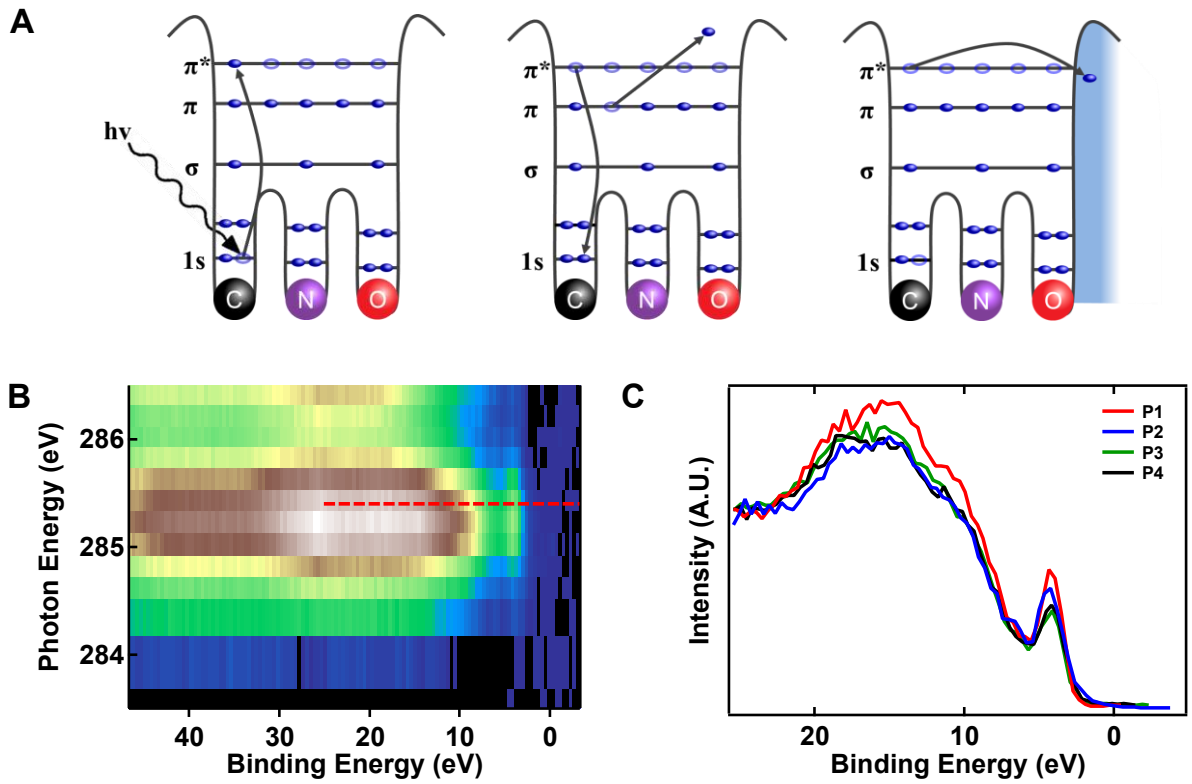

Figure 3.2: (A) Illustration of the promotion of a core electron to an unoccupied orbital (left), the relaxation of the excited electron *via* the participator decay process (middle), and the delocalization of the electron into the surrounding electronic environment (right). (B) A two-dimensional plot of the RPES intensity versus the photon energy and electron binding energy for a monolayer from P1. The red dashed line corresponds to the one-dimensional plot of the RPES intensity versus the electron binding energy for P1 in (C). (C) The normalized RPES intensity profiles for the P1 (red), P2 (blue), P3 (green), and P4 (black) monolayers. The data is extracted from the two-dimensional RPES intensity plots at photon energies of 285.4 eV, corresponding to the promotion of a carbon 1s core electron to the LUMO+1.

We next used the core-hole clock method to evaluate the intrinsic excited-state charge transfer times from the RPES plots obtained for backfilled monolayers from **P1**, **P2**, **P3**, and **P4**.[21,22,32-41] Figure 3.2C shows one-dimensional plots of the RPES intensity versus the electron binding energy for these monolayers at a photon excitation energy of 285.4 eV

(specifically corresponding to the promotion of a carbon 1s core electron to the LUMO+1).[57-59] By evaluating the quenching of the prominent participator decay between binding energies of 3.2 eV and 5.5 eV, we extracted the excited electron delocalization rates and hence the associated charge transfer times of 11.5 ± 1.5 fs, 8.4 ± 1.0 fs, 5.2 ± 0.5 fs, and 5.7 ± 0.6 fs for backfilled monolayers from **P1, P2**, **P3**, and **P4**, respectively (see the Supporting Information for calculation details).[21,22,32-41] Here, the observed charge transfer times generally *decreased* with increasing molecular length (i.e. greater number of PTCDI building blocks), with a substantial difference between monolayers from **P1** and monolayers from **P4** (Figure 3.3). The observed trend was surprising, as previous studies have explicitly demonstrated that charge transfer times roughly increase with length for nitrile- and ferrocene-terminated alkanethiol monolayers (in contrast to our findings).[60,61] Indeed, for the **P1** to **P4** series, the longer macromolecules extend farther from the surface and should be more poorly coupled with the substrate, hindering excited electron delocalization and presumably leading to an increase (rather than a decrease) in the observed charge transfer times.

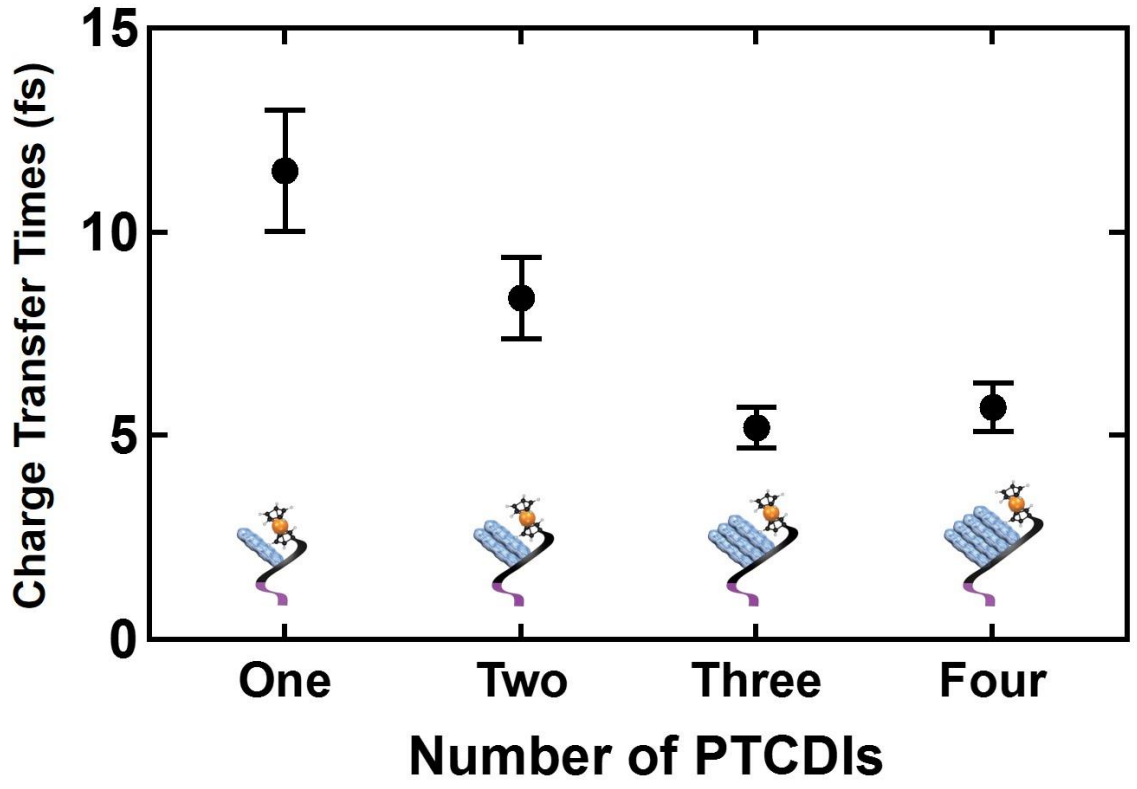

Figure 3.3: The calculated charge transfer times for **P1, P2, P3,** and **P4** (the illustrations of the corresponding macromolecules are inset). Note that the charge transfer times decrease as the length of the columnar molecular stack increases.

To understand our unexpected findings, we examined the electronic structure of the **P1** to **P4** series. For this purpose, we first used molecular dynamics simulations to obtain the equilibrium geometries of our macromolecules' PTCDI-based substructures[52,57] (Figures S2.12 and S2.13). We then employed density functional theory calculations to generate the shapes of their corresponding molecular orbitals, both in the ground state and with a core electron promoted to the LUMO+1 (Figures S3.6 and S3.7).[62-65] Interestingly, we noted that the electron density was delocalized over either the entirety or majority of our macromolecules' aromatic cores, as exemplified by the isosurface plots of their LUMO+1's

(Figures S3.6 and S3.7). In addition, we found that **P1**, **P2**, **P3**, and **P4** possessed LUMO+1 energies of approximately –0.9 eV, –2.9 eV, –3.2 eV, and –3.1 eV, respectively (note that these values are estimates, as our calculations employ functionals with limited accuracy and do not take into account solvent and substrate effects). Moreover, we observed that the longer macromolecules featured multiple closely-spaced unoccupied states at lower energies due to strong intermolecular interactions (Figure S3.8). Given the information from our calculations, the measured unexpected trend in the charge transfer times could be rationalized by considering the electron density delocalization and lower energies for the unoccupied orbitals of **P1**, **P2**, **P3**, and **P4**. This length-dependent evolution in our macromolecules' electronic properties likely facilitated the efficient transfer of the excited electrons into the surrounding environment.

3.4 Conclusion

In conclusion, we have quantified excited-state charge transfer dynamics at PTCDI-based model organic-inorganic interfaces, and our study holds significance for several reasons. First, the presented approach employs entrenched DNA synthesis and self-assembly techniques to produce well defined arrays of columnar stacks of organic semiconductor building blocks at solid substrates. Such precise control is difficult to achieve within traditional synthesis and self-assembly contexts, potentially making our strategy valuable for scientists working on understanding charge transfer phenomena. Second, the reported measurements reveal an unexpected trend in the rate of charge transfer from our macromolecules to their surroundings, which decreases, rather than increases, with molecular length. This trend can be rationalized by considering the

evolution in electronic structure that occurs when organic semiconductors transition from isolated molecules to extended solids. Third, our experiments provide access to charge transfer dynamics at electronically and structurally well-defined model interfaces with atomic-level chemical resolution and femtosecond-range temporal resolution. Given that core-level excited states share some common features with valence-level excited states for π-conjugated organic semiconductors,[66] our strategy may prove valuable for exploring interface-associated charge transfer dynamics in a broad range of carbon-based materials. Finally, the calculated charge transfer times of ~ 6 to ~ 12 fs measured for our DNA-like constructs are virtually identical to charge transfer times of ~ 6 fs measured for DNA under analogous conditions.[67,68] This direct comparison is interesting from the perspective of the DNA conductivity field and supports the classic notion that duplex DNA shares characteristics with one-dimensional aromatic crystals, further underscoring the general applicability of our work.[69-71] Altogether, the presented methodology may open new opportunities for the fundamental study of structure-function relationships in arbitrary organic materials, nanoscale charge transfer phenomena at device-relevant organic-inorganic interfaces, and conductivity in biological and bioinspired systems.

3.5 Supporting Information

3.5.1 General Information and Experimental Procedures

Information and general procedures for the synthesis of the macromolecules used in this study, the molecular dynamic simulations, and self-assembly onto gold substrates is provided in section 2.5 of this thesis.

3.5.2 X-ray Spectroscopy of the PTCDI-Based Mixed Monolayers and Multilayers

X-ray spectroscopy experiments were performed at the ALOISA beamline of the Elettra Synchrotron in Trieste, Italy in an ultra-high vacuum end station.[72] During the experiments, the sample temperature was maintained at –60 °C, thereby limiting molecular decompositions during irradiation and minimizing water adsorption, and the measurement and sample preparation chamber pressures were maintained at 10^{-11} mbar and 10^{-10} mbar, respectively. The backfilled monolayers and multilayers were characterized using resonant photoemission spectroscopy (RPES). The RPES experiments were performed by taking XPS scans (0 to 50 eV binding energy) at a series of incident photon energies across the entire range of the carbon K-edge ionization threshold (278 eV to 310 eV), with an overall energy resolution of ~ 400 meV. The surface was oriented at a grazing-incidence angle of 4˚ and roughly at P-polarization, with a hemispherical electron analyzer positioned 35˚ off the scattering plane (acceptance angle of 2°). The binding energy of the C1s RPES maps was calibrated relative to the Fermi energy by using substrate Fermi edge at 0 eV, or by using the carbon 1s XPS peak that resulted from the second order photon excitation. Note that for the photon energy that matches twice the carbon 1s binding energy, the second order carbon 1s peak appears in the RPES spectra at a binding energy of 0 eV. In addition, the absolute photon energy was calibrated a posteriori according to established literature procedures.[72] The data obtained for all of the measurements were analyzed and processed according to established literature procedures.[22,32,33,35-41,59]

3.5.3 Calculation of the Charge Transfer Times

The charge transfer dissociation times τ_{CT} for macromolecules **P1**, **P2**, **P3**, and **P4**

were calculated according to established literature protocols.[22,32,33,35-37,39,40,72] First, the non-resonant photoemission signal at energies below the C1s-LUMO excitation (the pre-edge) was subtracted from each of the corresponding two-dimensional RPES plots (Figures S3.1-S3.4). Subsequently, the resonant spectra were normalized to the overall Auger intensity above the ionization threshold of 310 eV, enabling a quantitative analysis of the intensity quenching for the HOMO participator decay peak. To facilitate comparisons of the relative charge transfer times, we extracted one-dimensional RPES intensity profiles for **P1**, **P2**, **P3**, and **P4** monolayers at a photon excitation energy of 285.4 eV, specifically corresponding to the promotion of a carbon 1s core electron to the LUMO+1 (Supporting Information Figures S3.1-S3.8). Note that the inelastic electron emission was modeled as a Shirley-type background and subtracted from each of these one-dimensional plots. Here, the participator intensities (I_p) of the valence band resonances for **P1**, **P2**, **P3**, and **P4** were then evaluated by integrating the peaks between 3.2 eV and 5.5 eV (i.e. the binding energy range of the HOMO), and the corresponding charge delocalization times were calculated by following the core-hole-clock approach[22,32,33,35-41,59] *via* the equation[32]

$$\tau_{CT} = \tau_{CH} \frac{I_{coupled}}{I_{isolated} - I_{coupled}}$$

where τ_{CH} = 6 fs is the reported core-hole lifetime for carbon 1s,[73] $I_{isolated}$ is the integrated participator intensity for a long-lived reference, and $I_{coupled}$ is the participator intensity for a mixed monolayer.[32] In accordance with literature procedures, we assumed that all aromatic carbon atoms were equally coupled to their surroundings and employed a PTCDI multilayer, for which the constituent molecules were poorly coupled to their surroundings, as the long-lived reference (Figure S3.5). The calculations yielded charge

transfer times of 11.5 ± 1.5 fs for the **P1** monolayer, 8.4 ± 1 fs for the **P2** monolayer, 5.2 ± 0.5 fs for the **P3** monolayer, and 5.7 ± 0.6 fs for the **P4** monolayer. Note that the errors were calculated by including the signal-to-noise ratio of the measured resonant spectra and the reported error of the carbon 1s core-hole lifetime.

3.5.4 Density-Functional Theory Calculations for the PTCDI-Based Macromolecules

Density functional theory (DFT) was used to predict the orbital shapes and energies for the subunits of macromolecules **P1**, **P2**, **P3**, and **P4**. The averaged structures obtained from the molecular dynamics simulations were used for the subunit geometries, and for computational simplicity, the DFT calculations employed constructs that were substituted with methyl groups (rather than hexaethyleneglycol monomethyl ether) at the imide positions opposite to the phosphate backbone (Figure S2.12). For the ground state, the shapes and energies of the molecular orbitals (Figure S3.6) were calculated within the Gaussian 09 package.[63] The orbitals were expanded in the cc-pVTZ basis set and the CAM-B3LYP exchange-correlation functional.[62] For the excited state in the presence of a core hole, the shapes of the molecular orbitals (Figure S3.7) were calculated within the Atomic Simulation Environment using GPAW a grid-based real-space projector-augmented-wave (PAW) code[64,65,74] and the Perdew Burke Ernzerhof (PBE) exchange-correlation functional.[75] In this calculation, the default grid spacing of 0.2 was found to be sufficient, and the convergence of the self-consistency cycle was used to preserve minimum box sizes. Note that a core hole was introduced within a carbon atom via the PAW pseudopotential for each macromolecule and an electron was placed in the LUMO+1 for the top PTCDI moiety of each macromolecule. All isosurface plots were rendered in VESTA.[76]

3.5.5 Supporting Figures

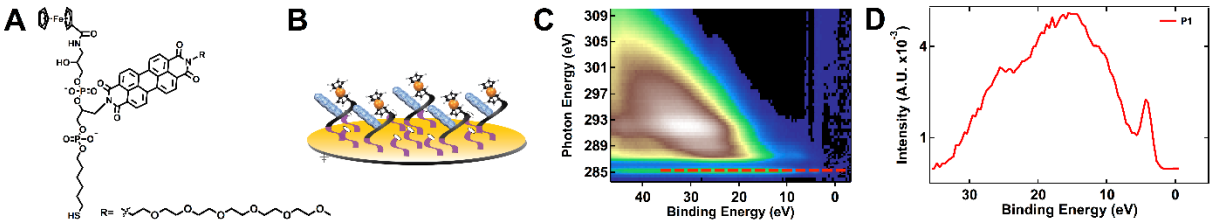

Figure S3.1: (A) Chemical structure of the **P1** macromolecule. (B) Illustration of a mixed monolayer from **P1**. (C) A two-dimensional plot of the signal intensity versus the photon energy and electron binding energy for a monolayer from **P1**. The dashed line corresponds to the one-dimensional plot of the signal intensity versus the electron binding energy in D. (D) The normalized resonant participator intensity profile for the **P1** monolayer at an incident photon energy of 285.4 eV.

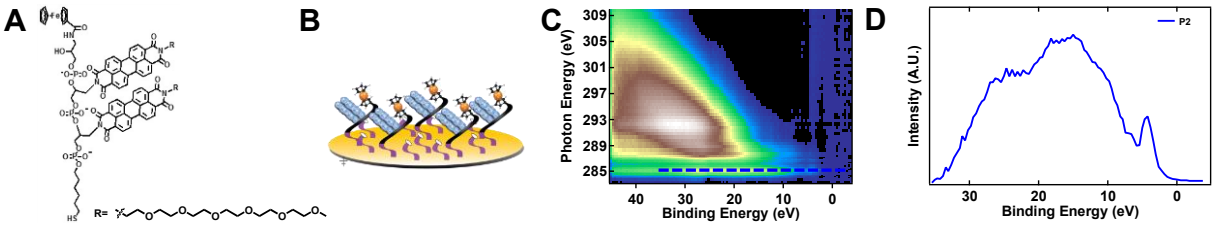

Figure S3.2: (A) Chemical structure of the **P2** macromolecule. (B) Illustration of a mixed monolayer from **P2**. (C) A two-dimensional plot of the signal intensity versus the photon energy and electron binding energy for a monolayer from **P2**. The dashed line corresponds to the one-dimensional plot of the signal intensity versus the electron binding energy in D. (D) The normalized resonant participator intensity profile for the **P2** monolayer at an incident photon energy of 285.4 eV.

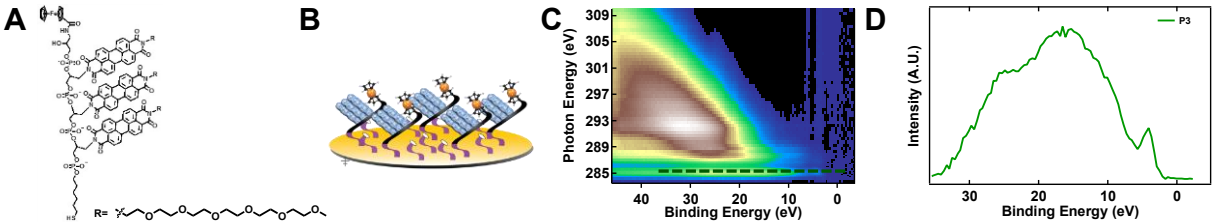

Figure S3.3: (A) Chemical structure of the **P3** macromolecule. (B) Illustration of a mixed monolayer from **P3**. (C) A two-dimensional plot of the signal intensity versus the photon energy and electron binding energy for a monolayer from **P3**. The dashed line corresponds to the one-dimensional plot of the signal intensity versus the electron binding energy in D. (D) The normalized resonant participator intensity profile for the **P3** monolayer at an incident photon energy of 285.4 eV.

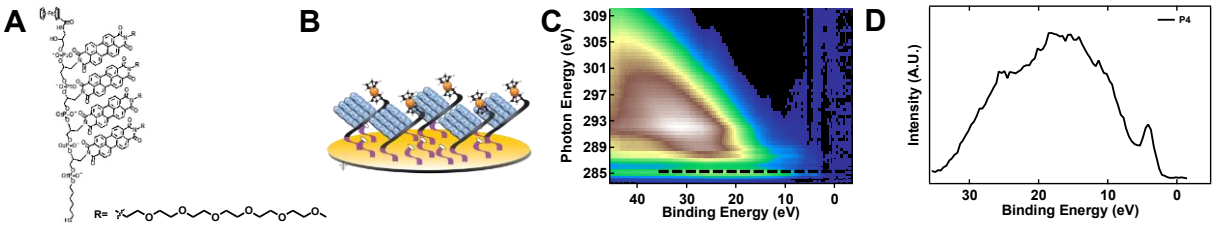

Figure S3.4: (A) Chemical structure of the **P4** macromolecule. (B) Illustration of a mixed monolayer from **P4**. (C) A two-dimensional plot of the signal intensity versus the photon energy and electron binding energy for a monolayer from **P4**. The dashed line corresponds to the one-dimensional plot of the signal intensity versus the electron binding energy in D. (D) The normalized resonant participator intensity profile for the **P4** monolayer at an incident photon energy of 285.4 eV.

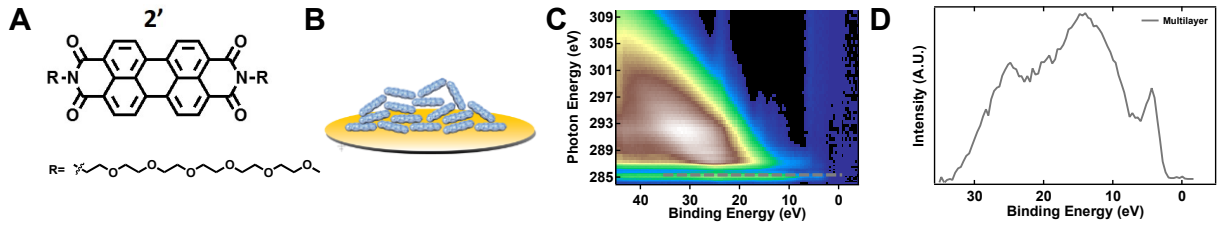

Figure S3.5. (A) Chemical structure of the small molecular PTCDI derivative **2'** used to form the multilayer. (B) Illustration of a multilayer from the small molecular PTCDI derivative. (C) A two-dimensional plot of the signal intensity versus the photon energy and electron binding energy for the PTCDI multilayer. The dashed line corresponds to the one-dimensional plot of the signal intensity versus the electron binding energy in D. (D) The normalized resonant participator intensity profile for PTCDI multilayer at an incident photon energy of 285.4 eV.

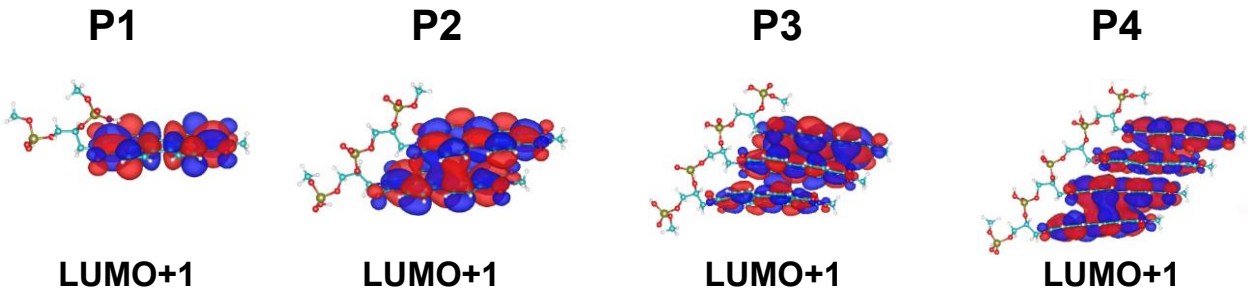

Figure S3.6: Isosurface plots for the LUMO + 1 of **P1**, **P2**, **P3**, and **P4** for the ground state in the absence of a core hole. The isosurface values for all of the plots have been set to 0.01 |e|/Å^3.

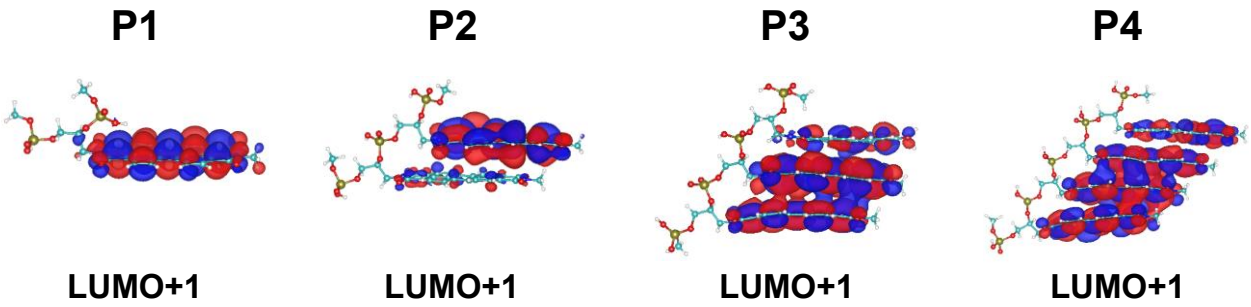

Figure S3.7: Isosurface plots for the LUMO + 1 of **P1**, **P2**, **P3**, and **P4** in the presence of a core hole and with an electron promoted to the orbital. The isosurface values for all of the plots have been set to 0.01 |e|/Å^3.

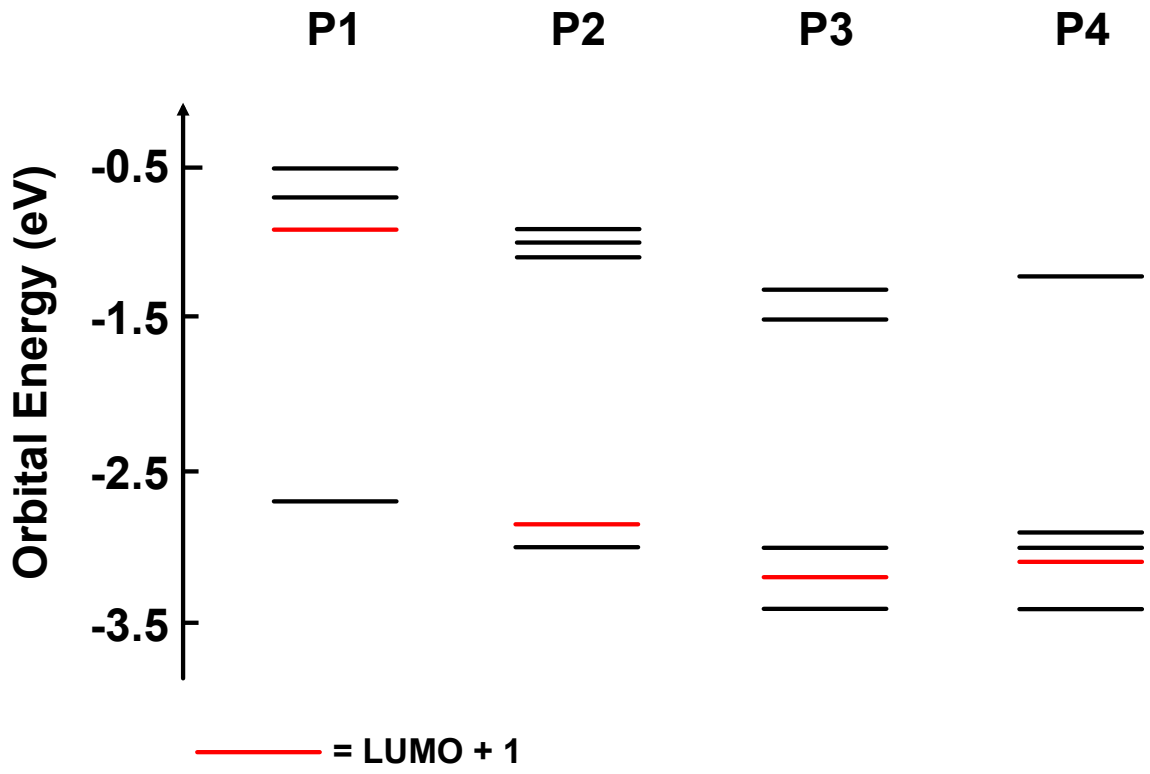

Figure S3.8. The theoretically determined energies of the LUMOs and energetically-similar unoccupied orbitals for **P1, P2, P3,** and **P4**. The LUMO+1 energy levels reported in the text are colored red. The energies correspond to the ground state calculations in the absence of a core hole, i.e. Figure S3.6.

3.6 References

1) H. Sirringhaus, *Adv. Mater.*, 2014, **26**, 1319.
2) K. Zhou, H. Dong, H.-L. Zhang, W. Hu, *Phys. Chem. Chem. Phys.*, 2014, **16**, 22448.
3) M. Gsänger, D. Bialas, L. Huang, M. Stolte, F. Würthner, *Adv. Mater.*, 2016, **28**, 3615.
4) W. Cao, J. Xue, *Energy Environ. Sci.*, 2014, **7**, 2123.
5) National Renewable Energy Laboratory "Best Research-Cell Efficiencies" http://www.nrel.gov/ncpv/images/efficiency_chart.jpg, (accessed December 2016).
6) G. Luo, X. Ren, S. Zhang, H. Wu, W. C. H. Choy, Z. He, Y. Cao, *Small*, 2016, **12**, 1547.
7) J.-H. Jou, S. Kumar, A. Agrawal, T.-H. Li, S. Sahoo, *J. Mater. Chem. C*, 2015, **3**, 2974.
8) S. Scholz, D. Kondakov, B. Lüssem, K. Leo, *Chem. Rev.*, 2015, **115**, 8449.
9) R.-P. Xu, Y.-Q. Li, J.-X. Tang, *J. Mater. Chem. C*, 2016, **4**, 9116.
10) J. Hwang, A. Wan, A. Kahn, *Mater. Sci. Eng. R*, 2009, **64**, 1.
11) S. Braun, W. R. Salaneck, M. Fahlman, *Adv. Mater.*, 2009, **21**, 1450.
12) C. Liu, Y. Xu, Y.-Y. Noh, *Mater. Today*, 2015, **18**, 79.

13) H. Lee, S. W. Cho, Y. Yi, *Cur. Appl. Phys.*, 2016, **16**, 1533.
14) C. Schubert, J. T. Margraf, T. Clark, D. M. Guldi, *Chem. Soc. Rev.*, 2015, **44**, 988.
15) M. Gilbert, B. Albinsson, *Chem. Soc. Rev.*, 2015, **44**, 845.
16) J. S. Ward, R. S. Nobuyasu, A. S. Batsanov, P. Data, A. P. Monkman, F. B. Dias, M. R. Bryce, *Chem. Commun.*, 2016, **52**, 2612.
17) D. Davydova, A. de la Cadena, D. Akimov, B. Dietzek, *Laser Photon. Rev.*, 2016, **10**, 62.
18) H. Okhita, S. Ito in *Organic Solar Cells*, Green Energy and Technology, ed. W. C. H. Choy, Springer-Verlag, London, England, 2013, 103–137.
19) S. D. Dimitrov, J. R. Durrant, *Chem. Mater.*, 2014, **26**, 616.
20) X.-Y. Zhu, *J. Phys. Chem. B*, 2004, **108**, 8778.
21) D. Menzel, *Chem. Soc. Rev.*, 2008, **37**, 2212.
22) L. Cao, X.-Y. Gao, A. T. S. Wee, D.-C. Qi, *Adv. Mater*., 2014, **26**, 7880.
23) A. Kahn, *Mater. Horiz.*, 2016, **3**, 7.
24) C. Sutton, C. Risko, J. L. Brédas, *Chem. Mater.*, 2016, **28**, 3.
25) J. Rivnay, S. C. B. Mannsfeld, C. E. Miller, A. Salleo, M. F. Toney, *Chem. Rev.*, 2012, **112**, 5488.
26) N. Ueno, in *Physics of Organic Semiconductors*, ed. W. Brutting, C. Adachi, Wiley-VCH, Weinheim, Germany, 2012, 65–90.
27) C. Huang, S. Barlow, S. R. Marder, *J. Org. Chem.*, 2011, **76**, 2386.
28) Y. Geng, H.-B. Li, S.-X. Wu, Z.-M. Su, *J. Mater. Chem.*, 2012, **22**, 20840.
29) D. Görl, X. Zhang, F. Würthner, *Angew. Chem., Int. Ed.,* 2012, **51**, 6328.
30) F. Würthner, C. R. Saha-Möller, B. Fimmel, S. Ogi, P. Leowanawat, D. Schmidt, *Chem. Rev.*, 2016, **116**, 962.
31) M. Sun, K. Müllen, M. Yin, *Chem. Soc. Rev.*, 2016, **45**, 1513.
32) P. A. Brühwiler, O. Karis, N. Mårtensson, *Rev. Mod. Phys.*, 2002, **74**, 703.
33) P. Vilmercati, D. Cvetko, A. Cossaro, A. Morgante, *Surf. Sci.*, 2009, **603**, 1542.
34) M. Zharnikov, *J. Electron. Spectrosc. Relat. Phenom.*, 2015, **200**, 160.
35) O. Björneholm, A. Nilsson, A. Sandell, B. Hernnäs, N. Mårtensson, *Phys. Rev. Lett.*, 1992, **68**, 1892.
36) M. Ohno, *Phys. Rev. B*, 1994, **50**, 2566.
37) O. Karis, A. Nilsson, M. Weinelt, T. Wiell, C. Puglia, N. Wassdahl, N. Mårtensson, M. Samant, J. Stöhr, *Phys. Rev. Lett.*, 1996, **76**, 1380.
38) L. Cao, Y.-Z. Wang, T.-X. Chen, W.-H. Zhang, X.-J. Yu, K. Ibrahim, J.-O. Wang, H.-J. Qian, F.-Q. Xu, D.-C. Qi, A. T. S. Wee, *J. Chem. Phys.*, 2011, **135**, 174701.
39) A. Batra, G. Kladnik, H. Vázquez, J. S. Meisner, L. Floreano, C. Nuckolls, D. Cvetko, A. Morgante, L. Venkataraman, *Nat. Commun.*, 2012, **3**, 1038.
40) T. Schiros, G. Kladnik, D. Prezzi, A. Ferretti, G. Olivieri, A. Cossaro, L. Floreano, A. Verdini, C. Schenck, M. Cox, A. A. Gorodetsky, K. Plunkett, D. Delongchamp, C. Nuckolls, A. Morgante, D. Cvetko, I. Kymissis, *Adv. Energ. Mater.*, 2013, **3**, 894.
41) L. Cao, Y.-Z. Wang, J.-Q. Zhong, Y.-Y. Han, W.-H. Zhang, X.-J. Yu, F.-Q. Xu, D.-C. Qi, A. T. S. Wee, *J. Phys. Chem. C*, 2014, **118**, 4160.
42) C. B. Reese, *Org. Biomol. Chem.*, 2005, **3**, 3851.
43) Y. N. Teo, E. T. Kool, *Chem. Rev.*, 2012, **112**, 4221.
44) S. Kosuri, G. M. Church, *Nat. Methods*, 2014,**11**, 499.
45) C. Wagner, H.-A. Wagenknecht, *Org. Lett.*, 2006, **8**, 4191.
46) D. Baumstark, H.-A. Wagenknecht, *Chem. Eur. J.*, 2008, **14**, 6640.

47) D. Baumstark, H.-A. Wagenknecht, *Angew. Chem., Int. Ed.*, 2008, **47**, 2612.
48) T. A. Zeidan, R. Carmieli, R. F. Kelley, T. M. Wilson, F. D. Lewis, M. R. Wasielewski, *J. Am. Chem. Soc.*, 2008, **130**, 13945.
49) M. Hariharan, Y. Zheng, H. Long, T. A. Zeidan, G. C. Schatz, J. Vura-Weis, M. R. Wasielewski, X. Zuo, D. M. Tiede, F. D. Lewis, *J*. *Am*. *Chem*. *Soc*., 2009, **131**, 5920.
50) T. M. Wilson, T. A. Zeidan, M. Hariharan, F. D. Lewis, M. R. Wasielewski, *Angew. Chem. Int. Ed.*, 2010, **49**, 2385.
51) C. H. Wohlgamuth, M. A. McWilliams, A. Mazaheripour, A. M. Burke, K.-Y. Lin, L. Doan, J. D. Slinker, A. A. Gorodetsky, *J. Phys. Chem. C*, 2014, **118**, 29084.
52) C. B, Markegard, A. Mazaheripour, J.-M. Jocson, A. M. Burke, M. N. Dickson, A. A. Gorodetsky, H. D. Nguyen, *J. Phys. Chem. B*, 2015, **119**, 11459.
53) J. C. Love, L. A. Estroff, J. K. Kriebel, R. G. Nuzzo, G. M. Whitesides, *Chem. Rev.*, 2005, **105**, 1103.
54) Q. Chi, M. J. Ford, A. Halder, N. S. Hush, J. R. Reimers, J. Ulstrup, *Curr. Opin. Electrochem*, 2017, **1**, 7.
55) A. A. Gorodetsky, M. C. Buzzeo, J. K. Barton, *Bioconjugate Chem.*, 2008, **19**, 2285.
56) T. Tang, B. Ge, D. Sen, H.-Z. Yu, *Chem. Soc. Rev.*, 2014, **43**, 518.
57) A. G. Wardrip, A. Mazaheripour, N. Hüsken, J.-M. Jocson, A. Bartlett, R. C. Lopez, N. Frey, C. B. Markegard, G. Kladnik, A. Cossaro, L. Floreano, A. Verdini, A. M. Burke, M. N. Dickson, I. Kymissis, D. Cvetko, A. Morgante, S. Sharifzadeh, H. D. Nguyen, A. A. Gorodetsky, *Angew. Chem. Int. Ed.*, 2016, **55**, 14267.
58) L. N. S. Loli, H. Hamoudi, J. E. Gayone, M. L. Martiarena, E. A. Sánchez, O. Grizzi, L. Pasquali, S. Nannarone, B. P. Doyle, C. Dablemont, V. A. Esaulov, *J. Phys. Chem. C.*, 2009, **113**, 17866.
59) G. Fratesi, V. Lanzilotto, S. Stranges, M. Alagia, G. P. Brivio, L. Floreano, *Phys. Chem. Chem. Phys.*, 2014, **16**, 14834.
60) P. Kao, S. Neppl, P. Feulner, D. L. Allara, M. Zharnikov, *J. Phys. Chem. C*, 2010, **114**, 13766.
61) L. Cao, M. Yang, L. Yuan, N. Nerngchamnong, Y.-P. Feng, A. T. S. Wee, D.-C. Qi, C. A. Nijhuis, *J. Phys.: Condens. Matter*, 2016, **28**, 094006.
62) T. Yanai, D. P. Tew, N. C. Handy, *Chem. Phys. Lett.*, 2004, **393**, 51.
63) M. J. Frisch, G. W. Trucks, H. B. Schegel, G. E. Scuseria, M. A. Robb, J. R. Cheeseman, G. Scalmani, V. Barone, B. Mennucci, G. A. Petersson, H. Nakatsuji, M. Caricato, X. Li, H. P. Hratchian, A. F. Izmaylov, J. Bloino, G. Zheng, J. L. Sonnenberg, M. Hada, M. Ehara, K. Toyota, R. Fukuda, J. J. Hasegawa, M. Ishida, T. Nakajima, Y. Honda, O Kitao, H. Nakai, T. Vreven, J. A. Montgomery, Jr., J. E. Peralta, F. Ogliaro, M. Bearpark, J. J. Heyd, E. Brothers, K. N. Kudin, V. N. Staroverov, R. Kobayashi, J. Normand, K. Raghavachari, A. Rendell, J. C. Burant, S. S. Iyengar, J. Tomasi, M. Cossi, N. Rega, J. M. Millam, M. Klene, J. E. Knox, J. B. Cross, V. Bakken, C. Adamo, J. Jaramillo, R. Gomperts, R. E. Stratmann, O. Yazyev, A. J. Austin, R. Cammi, C. Pomelli, J. W. Ochterski, R. L. Martin, K. Morokuma, V. G. Zakrzewski, G. A. Voth, P. Salvador, J. J. Dannenberg, S. Dapprich, A. D. Daniels, Ö. Farkas, J. B. Foresman, J. V. Ortiz, J. Cioslowski, D. J. Fox, Gaussian 09 (Revision D.01), Gaussian, Inc., Wallingford, CT, 2009.
64) J. J. Mortensen, L. B. Hansen, K. W. Jacobsen, *Phys. Rev. B*, 2005, **71**, 035109.
65) J. Enkovaara, C. Rostgaard, J. J. Mortensen, J. Chen, M. Dułak, L. Ferrighi, J. Gavnholt, C. Glinsvad, V. Haikola, H. A. Hansen, H. H. Kristoffersen, M. Kuisma, A. H. Larsen, L. Lehtovaara, M. Ljungberg, O. Lopez-Acevedo, P. G. Moses, J. Ojanen, T. Olsen, V. Petzold,

N. A. Romero, J. Stausholm-Møller, M. Strange, G. A. Tritsaris, M. Vanin, M. Walter, B. Hammer, H. Häkkinen, G. K. H. Madsen, R. M. Nieminen, J. K. Nørskov, M. Puska, T. T. Rantala, J. Schiøtz, K. S. Thygesen, K. W. Jacobsen, *J. Phys.: Condens. Matter*, 2010, **22**, 253202.
66) J. Schnadt, J. Schiessling, P. A. Brühwiler, *Chem. Phys.*, 2005, **312**, 39.
67) H. S. Kato, M. Furukawa, M. Kawai, M. Taniguchi, T. Kawai, T. Hatsui, N. Kosugi, *Phys. Rev. Lett.*, 2004, **93**, 086403.
68) L. Wang, K.-Q. Zhang, X. Gao, X.-Y. Liu, A. T. S. Wee, *Appl. Phys. Lett.*, 2006, **89**, 013902.
69) N. B. Muren, E. D. Olmon, J. K. Barton, *Phys. Chem. Chem. Phys.*, 2012, **14**, 13754.
70) A. R. Arnold, M. A. Grodick, J. K. Barton, *Cell Chem. Biol.*, 2016, **23**, 183.
71) D. Eley, D. I. Spivey, *Trans Faraday Soc.*, 1962, **58**, 411.
72) L. Floreano, G. Naletto, D. Cvetko, R. Gotter, M. Malvezzi, L. Marassi, A. Morgante, A. Santaniello, A. Verdini, F. Tommasini, G. Tondello, *Rev. Mod. Phys.*, 2002, **74**, 703.
73) M. Coville, T. D. Thomas, *Phys. Rev. A*, 1991, **43**, 6053.
74) S. R. Bahn, K. W. Jacobsen, *Comput. Sci. Eng.*, 2002, **4**, 56.
75) J. P. Perdew, K. Burke, M. Ernzerhof, *Phys. Rev. Lett.* 1996, **77**, 3865.
76) K. Momma, F. Izumi, *J. Appl. Crystallogr.*, 2001, **44**, 1272.

CHAPTER 4 Summary and Future Work

4.1 Summary

To summarize, this work offers a pathway for the design and discovery of a novel class of one-dimensional bioinspired organic molecular wires for which the position of every chemical group is precisely defined. To obtain such molecular wires, we used scalable and robust chemical synthesis protocols adapted from bioconjugate chemistry, enabling us to merge the biological building block assembly strategy of DNA with the desirable physical characteristics of well known organic semiconductors. We can confirm that the obtained polymeric hybrid functional materials possess controllable architectures and precisely-defined morphologies at solid substrates with a suite of robust physical characterization techniques. By further evaluating the charge transport properties of these model one-dimensional molecular wires with electrochemical, x-ray spectroscopic, and computational methods, we will develop the knowledge base necessary for the discovery, design, and synthesis of novel organic electronic functional materials for next-generation electronic devices.

4.2 Future Work

Since we have established our integrated methodology for the synthesis, purification, structural characterization, x-ray spectroscopic interrogation, electrochemical investigation, and computational analysis of organic molecular wires from one specific building block, we will rationally design and investigate their sequence-variable analogues. For our new molecular wires, we will specifically focus on PTCDIs for which precursors are commercially available (or furnished from other commercial molecules in one synthetic

step); are fully compatible with the described synthetic methods and general self-assembly strategies; and feature well-defined changes in their electrochemical/electronic properties due to substituents on their aromatic cores.[16-20] Figure 4.1A shows the core-unsubstituted PTCDI used for our preliminary experiments and several core-substituted PTCDIs that satisfy the aforementioned criteria. Indeed, PTCDIs with strongly electron-withdrawing cyano substituents on their aromatic cores are easier to reduce by ~ 0.3 V, as well as more difficult to oxidize, and PTCDIs with strongly electron-donating pyrrolidino substituents on their aromatic cores are more difficult to reduce by ~ 0.3 V, as well as easier to oxidize by ~ 1.0 V.[16,17,19,20] For one potential set of studies, we will design the sequence-variable organic molecular wires illustrated in Figure 4.1B that will feature identical lengths but will be comprised of distinct core-substituted PTCDI building blocks. Such constructs will enable the investigation of charge transport in multiple analogous systems, providing insight into how even subtle molecular-level structural changes influence the functionality of one-dimensional models of pi-stacked organic semiconductor ensembles. For another potential set of studies, we will design the organic molecular wires illustrated in Figure 4.1C that incorporate distinct segments from core-unsubstituted PTCDIs, which are a p-type material,[16,17,19,20] and pyrrolidino-substituted PTCDIs, which are an n-type material,[16,17,19,20] in one-dimensional models of p-n, p-n-p, or n-p-n junctions. Such constructs will enable the investigation of charge transport across one-dimensional models of organic/organic heterostructures (which play crucial roles in the performance of organic light emitting diodes and solar cells),[1-15] providing insight into charge separation mechanisms within pi-stacked organic semiconductor ensembles. For a final potential set of studies, we will design the organic molecular wires illustrated in Figure 4.1D, for which a single core-

substituted PTCDI is placed at different specified positions within a larger segment of core-unsubstituted PTCDIs. Such constructs will enable the investigation of charge transport in the presence of chemical defects (corresponding to the PTCDIs' core substituents), providing insight into how a small number of impurities affect the migration and/or trapping of charge in one-dimensional models of otherwise pristine materials.[1-15] This approach will be completely general, enabling the design (and eventual investigation) of a wide variety of unique and unprecedented precisely-defined systems that would not be possible outside the proposed methodology.

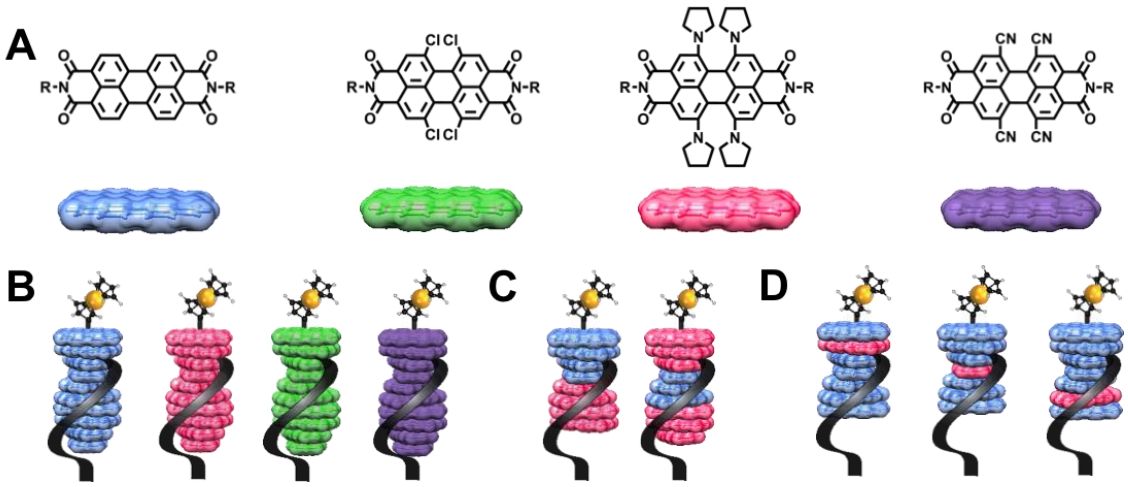

Figure 4.1: (A) Chemical structures (top) and cartoon representations (bottom) for core-unsubstituted, chloro-substituted, pyrrolidino-substituted, and cyano-substituted PTCDI building blocks. (B) Cartoon representations of molecular wires with identical lengths but from different PTCDI building blocks. (C) Cartoon representations of molecular wires from two different building blocks that result in a nanoscale p-n junction (left) and n-p-n junction (right). (D) Cartoon representations of molecular wires from two different building blocks, where a tract from one PTCDI variant features another derivative at different locations as a de facto defect.

Finally, this work is exciting from the perspective of benchmarking our materials' emergent properties against classical concepts from the literature. By preparing and characterizing a series of length-variable constructs from molecular building blocks, we can directly observe the changes in electronic structure accompanying the transition of an isolated molecule to a material, as illustrated in Figure 1.1A, along with the consequences of this transition for charge transport. Through analogous studies on molecular wires containing organic/organic heterostructures, such as the p-n and n-p-n junctions in Figure 4.1C, or on constructs containing different building blocks at precisely defined positions, such as the sequence-variable constructs in Figure 4.1D, we can gain unprecedented insight into nanoscale interfacial charge transfer phenomena for both pristine and defect-containing systems. Moreover, due to their phospho-alkane backbone and aromatic building block spacing, our molecular wires will share clear and common features with DNA. The proposed studies will thus enable a reassessment of the classic notion that duplex DNA shares characteristics with one-dimensional aromatic crystals,[22,23,24,25] underscoring the general relevance of our methodology. Altogether, the proposed work will provide exciting opportunities for the investigation and evaluation of structure-function relationships and charge transport phenomena across a broad range of molecular, organic, and biological systems.

4.3 References

1) Sirringhaus, H. 25th Anniversary Article: Organic Field-Effect Transistors: The Path Beyond Amorphous Silicon. *Adv. Mater.* **2014**, *26* (9), 1319–1335.
2) Dong, H.; Fu, X.; Liu, J.; Wang, Z.; Hu, W. 25th Anniversary Article: Key Points for High-Mobility Organic Field-Effect Transistors. *Adv. Mater.* **2013**, *25* (43), 6158–6183.

3) Dou, L.; You, J.; Hong, Z.; Xu, Z.; Li, G.; Street, R. A.; Yang, Y. 25th Anniversary Article: A Decade of Organic/Polymeric Photovoltaic Research. *Adv. Mater.* **2013**, *25* (46), 6642–6671.
4) National Renewable Energy Laboratory Best Research-Cell Efficiencies http://www.nrel.gov/ncpv/images/efficiency_chart.jpg, (accessed Aug 1, 2015).
5) Hwang, J.; Wan, A.; Kahn, A. Energetics of Metal–organic Interfaces: New Experiments and Assessment of the Field. *Mater. Sci. Eng. R Reports* **2009**, *64* (1–2), 1–31.
6) Braun, S.; Salaneck, W. R.; Fahlman, M. Energy-Level Alignment at Organic/metal and Organic/organic Interfaces. *Adv. Mater.* **2009**, *21* (14–15), 1450–1472.
7) Liu, C.; Xu, Y.; Noh, Y. Y. Contact Engineering in Organic Field-Effect Transistors. *Mater. Today* **2015**, *18* (2), 79–96.
8) Cropceanu, V.; Cornil, J.; da Silva Filho, D. A.; Olivier, Y.; Silbey, R.; Bredas, J.-L. Charge Transport in Organic Semiconductors. *Chem. Rev.* **2007**, *107*, 926–952.
9) Kymissis, I. *Organic Field Effect Transistors: Theory, Fabrication, and Characterization*; Springer: New York, **2009**.
10) Tessler, N.; Preezant, Y.; Rappaport, N.; Roichman, Y. Charge Transport in Disordered Organic Materials and Its Relevance to Thin-Film Devices: A Tutorial Review. *Adv. Mater.* **2009**, *21* (27), 2741–2761.
11) Kim, F. S.; Ren, G.; Jenekhe, S. A. One-Dimensional Nanostructures of π-Conjugated Molecular Systems: Assembly, Properties, and Applications from Photovoltaics, Sensors, and Nanophotonics to Nanoelectronics. *Chem. Mater.* **2011**, *23* (3), 682–732.
12) Rivnay, J.; Mannsfeld, S. C. B.; Miller, C. E.; Salleo, A.; Toney, M. F. Quantitative Determination of Organic Semiconductor Microstructure from the Molecular to Device Scale. *Chem. Rev.* **2012**, *112* (10), 5488–5519.
13) *Physics of Organic Semiconductors*; Brütting, W., Adachi, C., Eds.; Wiley-VCH Verlag GmbH & Co. KGaA: Weinheim, Germany, **2013**.
14) Puniredd, S. R.; Pisula, W.; Müllen, K. Influence of film morphology on optical and electronic properties of organic materials. in *Handbook of Organic Materials for Optical and (Opto)Electronic Devices,* Ostroverkhova, O., Ed.; Philadelphia, 2013, 83–101.
15) Köhler, A.; Bässler, H. *Electronic Processes in Organic Semiconductors: An Introduction*; Wiley-VCH: Weinheim, Germany, 2015.
16) Huang, C.; Barlow, S.; Marder, S. R. Perylene-3,4,9,10-Tetracarboxylic Acid Diimides: Synthesis, Physical Properties, and Use in Organic Electronics. *J. Org. Chem.* **2011**, *76* (8), 2386–2407.
17) Würthner, F.; Saha-Möller, C. R.; Fimmel, B.; Ogi, S.; Leowanawat, P.; Schmidt, D. Perylene Bisimide Dye Assemblies as Archetype Functional Supramolecular Materials. *Chem. Rev.* **2016**, *116* (3), 962–1052.
18) Sun, M.; Müllen, K.; Yin, M. Water-Soluble Perylenediimides: Design Concepts and Biological Applications. *Chem. Soc. Rev.* **2016**, *45* (6), 1513–1528.
19) Geng, Y.; Li, H.-B.; Wu, S.-X.; Su, Z.-M. The Interplay of Intermolecular Interactions, Packing Motifs and Electron Transport Properties in Perylene Diimide Related Materials: A Theoretical Perspective. *J. Mater. Chem.* **2012**, *22* (39), 20840-20851
20) Würthner, F. Perylene Bisimide Dyes as Versatile Building Blocks for Functional Supramolecular Architectures. *Chem. Commun.* **2004**, 1564–1579.
21) Tao, F.; Bernasek, S. L. Understanding Odd−Even Effects in Organic Self-Assembled Monolayers. *Chem. Rev.* **2007**, *107* (5), 1408–1453.

22) Gorodetsky, A. A.; Buzzeo, M. C.; Barton, J. K. DNA-Mediated Electrochemistry. *Bioconjug. Chem.* **2008**, *19* (12), 2285–2296.
23) Barton, J. K.; Furst, A. L.; Grodick, M. A. DNA Sensors Using DNA Charge Transport Chemistry. in DNA in *Supramolecular Chemistry and Nanotechnology*, Stultz, E.; Clever, G. H., Ed.; Wiley, 2015, 105–120.
24) Slinker, J. D.; Muren, N. B.; Renfrew, S. E.; Barton, J. K. DNA Charge Transport over 34 nm. *Nat. Chem.* **2011**, *3* (3), 228–233.
25) Guo, X.; Gorodetsky, A. A.; Hone, J.; Barton, J. K.; Nuckolls, C. Conductivity of a Single DNA Duplex Bridging a Carbon Nanotube Gap. *Nature Nanotechnol.* **2008**, *3*, 163–167.